

# Effect of energetic ions on edge-localized modes in tokamak plasmas

Received: 29 August 2022

Accepted: 9 October 2024

Published online: 06 January 2025

 Check for updates

J. Dominguez-Palacios<sup>1</sup>✉, S. Futatani<sup>2</sup>, M. Garcia-Munoz<sup>1</sup>✉, A. Jansen van Vuuren<sup>1,86</sup>, E. Viezzer<sup>1</sup>, J. Gonzalez-Martin<sup>1,3,87</sup>, M. Toscano-Jimenez<sup>1</sup>, P. Oyola<sup>1</sup>, Y. Todo<sup>4</sup>, Y. Suzuki<sup>5</sup>, L. Sanchis<sup>1,6,87</sup>, J. Rueda-Rueda<sup>1</sup>, J. Galdon-Quiroga<sup>1</sup>, J. Hidalgo-Salaverri<sup>1</sup>, H. Chen<sup>1,88</sup>, J. F. Rivero-Rodriguez<sup>7</sup>, L. Velarde<sup>1</sup>, the ASDEX Upgrade Team\* & the EuroFUSION MST1 Team\*

The most efficient and promising operational regime for the International Thermonuclear Experimental Reactor tokamak is the high-confinement mode. In this regime, however, periodic relaxations of the plasma edge can occur. These edge-localized modes pose a threat to the integrity of the fusion device. Here we reveal the strong impact of energetic ions on the spatio-temporal structure of edge-localized modes in tokamaks using nonlinear hybrid kinetic–magnetohydrodynamic simulations. A resonant interaction between the fast ions at the plasma edge and the electromagnetic perturbations from the edge-localized mode leads to an energy and momentum exchange. Energetic ions modify, for example, the amplitude, frequency spectrum and crash timing of edge-localized modes. The simulations reproduce some observations that feature abrupt and large edge-localized mode crashes. The results indicate that, in the International Thermonuclear Experimental Reactor, a strong interaction between the fusion-born alpha particles and ions from neutral beam injection, a main heating and fast particle source, is expected with predicted edge-localized mode perturbations. This work advances the understanding of the physics underlying edge-localized mode crashes in the presence of energetic particles and highlights the importance of including energetic ion kinetic effects in the optimization of edge-localized mode control techniques and regimes that are free of such modes.

On the road to a magnetic fusion power plant, a good confinement of a burning plasma, at temperatures  $>10^8$  K and particle densities  $>10^{20}$  m<sup>-3</sup>, is mandatory. In tokamaks, these conditions are typically achieved in the high-confinement regime (H-mode)<sup>1</sup>. The H-mode has been selected as the most efficient and promising operational regime for the International Thermonuclear Experimental Reactor (ITER), which is planned to start operation within the next decade and should prove the scientific and technical feasibility of magnetic confinement fusion. H-modes are, however, characterized by steep edge pressure gradients that are accompanied by periodic edge plasma relaxations

in the form of edge-localized modes (ELMs)<sup>2</sup> that, if allowed to grow unabated, can severely damage the first wall of ITER and future fusion power plants<sup>3</sup>. Extensive efforts are dedicated towards the development of ELM control techniques and ELM-free high-performance regimes<sup>3–10</sup>. Linear magnetohydrodynamic (MHD) stability analyses indicate that ELMs are coupled peeling–ballooning modes driven by the plasma edge current and pressure gradients<sup>11–14</sup>. Nonlinear MHD models successfully reproduce some relevant experimental observations such as ELM cycles<sup>15</sup>, filamentary structure<sup>16–18</sup> and collapse of the edge pressure profile<sup>19</sup>.

A full list of affiliations appears at the end of the paper. ✉ e-mail: [jdominguezpalacios@us.es](mailto:jdominguezpalacios@us.es); [mgm@us.es](mailto:mgm@us.es)

However, a detailed understanding of the ELM behaviour and consequences in a burning plasma with a notable fraction of energetic (suprathermal) ions is missing. Energetic ions are an essential source of momentum and energy that must be kept well confined until they slow down to the bulk plasma through Coulomb collisions<sup>20–22</sup>. Nevertheless, energetic ions are prone to show a rich variety of wave–particle interactions due to their large velocities and long mean free paths that can lead to an efficient exchange of energy and momentum with a broad spectrum of MHD fluctuations<sup>23–27</sup>. In fact, ELM-induced fast-ion losses are routinely observed in several tokamaks<sup>28</sup> with scintillator-based fast-ion loss detectors (FILDs)<sup>29</sup>. Recent FILD observations of fast-ion acceleration during ELM crashes in the Axially Symmetric Divertor Experiment) Upgrade (AUG) tokamak highlight the strong interplay between the energetic particle population at the plasma edge and the electromagnetic perturbation developed during an ELM crash<sup>30</sup>. Moreover, many of the natural no-ELM or small-ELM regimes, such as the Enhanced D-Alpha high-confinement mode<sup>31</sup> or type-II ELM regime (more recently dubbed quasi-continuous exhaust regime)<sup>32,33</sup>, feature plasmas with high collisionalities and, thus, negligible energetic particle contents. Extended Data Fig. 1 shows the plasma density perturbation during an ELM crash modelled with the MEGA code<sup>34</sup> together with a typical fast-ion orbit (in white) at the edge of the AUG tokamak. Eventually, its orbit ends on the wall and deposits its energy at the plasma facing component. A good understanding of the interaction between energetic ions and ELMs is, thus, of paramount importance to optimize ELM control techniques while minimizing fast-ion losses.

The three-dimensional nonlinear hybrid kinetic–MHD code MEGA has been used to self-consistently model an ELM crash in the presence of a realistic energetic ion distribution. These simulations provide evidence of the key role that energetic ion kinetic effects play in the spatio-temporal structure of ELMs. The wave–particle resonances are responsible for the net energy exchange between fast ions and ELMs. Comparisons of experimental measurements of the magnetic perturbations and fast-ion losses induced by large type-I ELMs are in qualitative agreement with the simulations. The results presented here provide a better understanding of the physics underlying an ELM crash in the presence of energetic particles and contribute to developing robust ELM control techniques and/or ELM-free regimes for future burning plasmas with fusion-born alpha particles.

## Experiments show that ELM and energetic particle dynamics are linked

The experiment analysed here has been performed with toroidal magnetic field  $B_t = 2.5$  T, plasma current  $I_p = 0.8$  MA, low collisionality ( $\nu_i^* < 0.5$  inside the pedestal top, where  $\nu_i^*$  is the ion collisionality, defined as the effective collision frequency normalized to the trapped particle bounce frequency) and 5 MW of neutral beam injection (NBI) as the main heating and fast-particle source.

Figure 1a shows an ELM-synchronized spectrogram of the radial magnetic field fluctuations ( $\partial B_r/\partial t$ ) measured with a Mirnov coil at the tokamak first wall for a plasma discharge with fast ions. In the experiment, the pre-ELM crash phase is characterized by a broadband frequency up to  $\sim 150$  kHz but dominated by low frequencies well below 50 kHz. The ELM crash itself (at  $t = 0$  ms) appears with a substantially larger perturbation amplitude and broadband frequency up to  $\sim 300$  kHz. Right after the ELM crash ( $t \approx 1.8$ – $3.5$  ms), the magnetic perturbation relaxes in amplitude and the frequency drops to  $f < 50$  kHz. The main features observed here in the ELM magnetic spectrograms are, in fact, ubiquitous to most tokamak H-mode plasmas<sup>35,36</sup>. Figure 1b,c shows the spectrogram and temporal evolution, respectively, of the fast-ion losses measured during the ELM crashes shown in Fig. 1a. The FILD spectrogram shows striking similarities to the magnetic spectrogram. Whereas during the pre-ELM crash phase, low frequencies up to  $\sim 100$  kHz dominate the spectrogram, during the

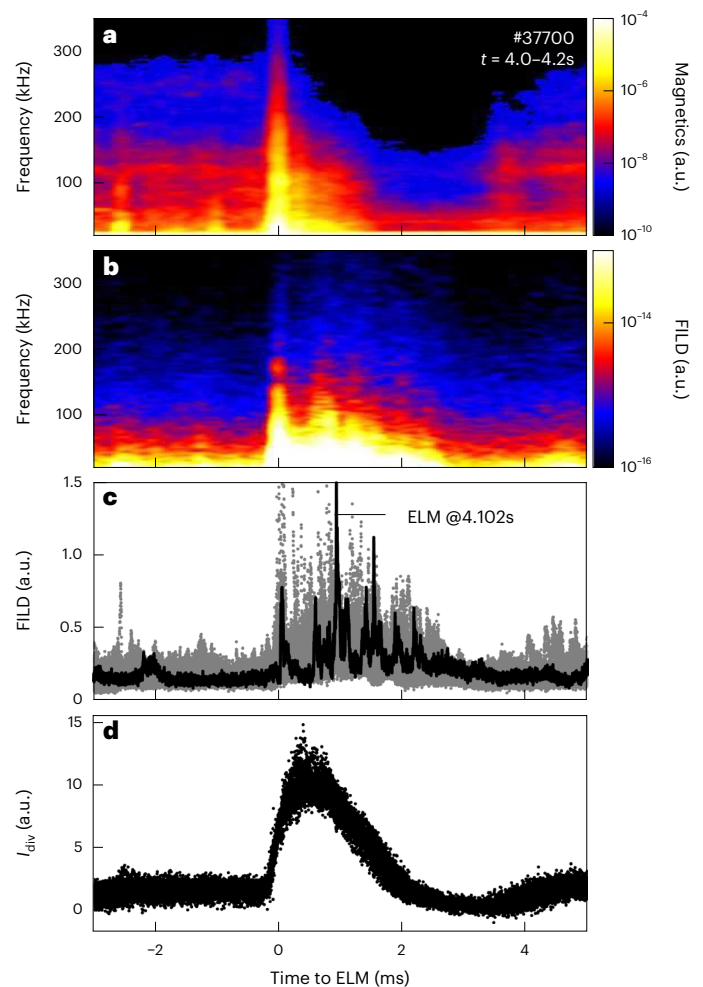


**Fig. 1 | ELM crash in AUG shot #37700.** **a, b**, ELM-synchronized spectrograms of measured radial magnetic field fluctuations ( $\partial B_r/\partial t$ , labelled as magnetics) for a plasma discharge with fast ions (**a**) and fast-ion losses at the low field side (LFS) midplane measured by the FILD (**b**), both for  $t = 4.0$ – $4.2$  s. **c**, The temporal evolution of the measured ELM-induced fast-ion losses (grey) during the time window used for the spectrograms shown in **a** and **b**, with the losses observed during a single ELM at  $t = 4.102$  s highlighted in black. **d**, Thermal particle losses measured by  $I_{\text{div}}$ , that is, the thermo-currents flowing through the outer divertor.

ELM crash, large-amplitude high-frequency (up to  $\sim 300$  kHz) losses are observed.

The amplitude of the high-frequency losses during the ELM crash decays to their nominal levels before the ELM crash in about 2–3 ms in the experiment presented here. Figure 1c shows the time traces of the fast-ion losses used to construct the FILD spectrogram (in grey) with that of a single ELM highlighted in black. Several fast-ion bursts (filaments) are commonly observed during each ELM. Finally, Fig. 1d shows the thermal particle losses measured by the thermo-currents flowing through the outer divertor during the ELMs. While the maximum thermal particle losses peak slightly after the ELM crash in the magnetic or FILD spectrogram, the thermal particle losses decay with the same time scale as the high-frequency fast-ion losses in the ELM-synchronized FILD spectrogram.

## Simulated ELM crash in the presence of energetic particles

To understand the experimental observations, the nonlinear interaction between energetic ions and ELMs has been modelled using the hybrid kinetic–MHD code MEGA with realistic plasma equilibrium, thermal particle profiles and off-axis NBI energetic particle distributions,

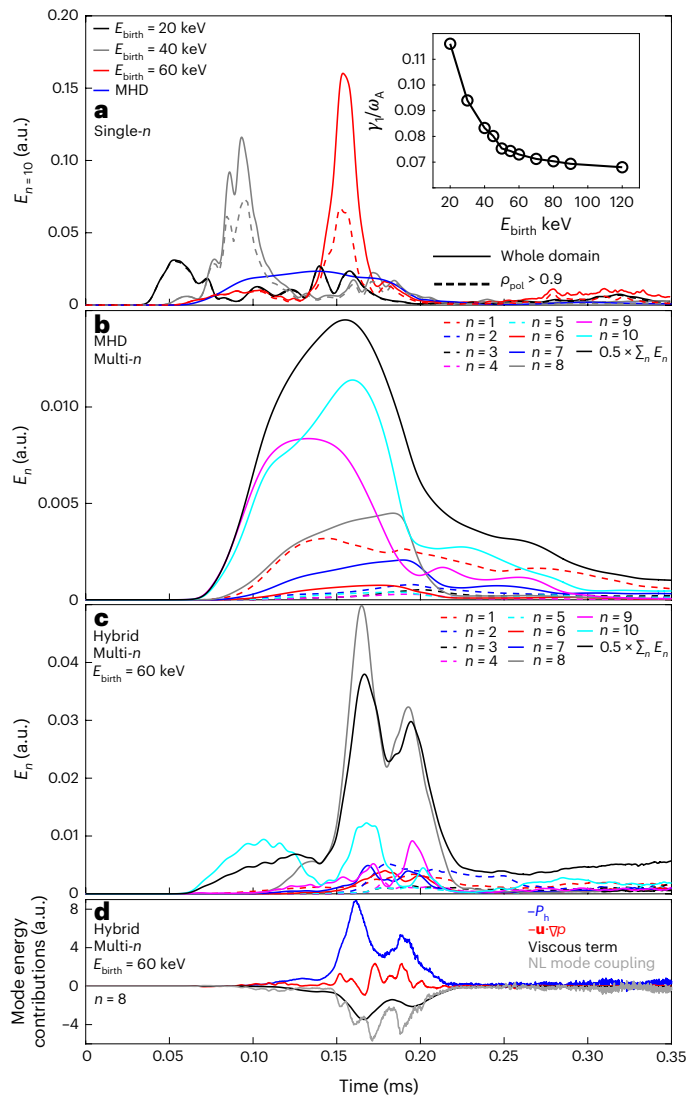


**Fig. 2 | Simulated ELM crash.** **a**, The time evolution of  $n = 10$  toroidal mode energy ( $E_{n=10}$ ) in single- $n$  simulations ( $n$  denotes the toroidal mode number). The solid line corresponds to integration in the whole simulation domain and the dashed line to integration from the radial coordinate  $\rho_{\text{pol}} > 0.9$ . The case without fast ions (blue solid) is shown for reference. Inset: the linear growth rate ( $\gamma_n$ , normalized to the Alfvén frequency at the magnetic axis,  $\omega_A$ ) versus NBI energy ( $E_{\text{birth}}$ ). **b, c**, The time evolution of each mode energy ( $E_n$ ) and of the sum of the mode energies ( $\sum_n E_n$ , multiplied by 0.5) in multi- $n$  MHD (**b**) and hybrid (for  $E_{\text{birth}} = 60$  keV) (**c**) simulations. **d**, Different contributions to  $E_{n=8}$  temporal evolution in the hybrid multi- $n$  simulation shown in **c**.  $P_h$  (blue) denotes the energy transfer between  $n = 8$  mode and energetic particles. The thermal plasma pressure gradient (red) is the volume integral of  $\mathbf{u} \cdot \nabla p$  (dot product between plasma velocity and thermal plasma pressure gradient). ‘Viscous term’ is the dissipation brought by viscosity (black), and ‘NL mode coupling’ corresponds to the energy transfer between  $n = 8$  and the rest of the toroidal modes (grey).

as seen in Extended Data Fig. 2. The simulation setup is described in Methods. The temporal evolution of the  $n = 10$  ( $n$  denotes the toroidal mode number) mode energy (kinetic + magnetic)<sup>37</sup> for a MHD single- $n$  (including only  $n = 0$  and 10 modes) simulation, that is, without fast ions, and three hybrid single- $n$  simulations with different NBI injection energies (denoted by  $E_{\text{birth}}$  hereafter) is shown in Fig. 2a. As shown in the inset, the linear growth rate of the mode decreases when  $E_{\text{birth}}$  is increased, which delays the ELM crash. During the nonlinear phase of the hybrid kinetic–MHD simulations, the ballooning mode extends to inner regions (radial coordinate,  $\rho_{\text{pol}} < 0.9$ ) and the mode

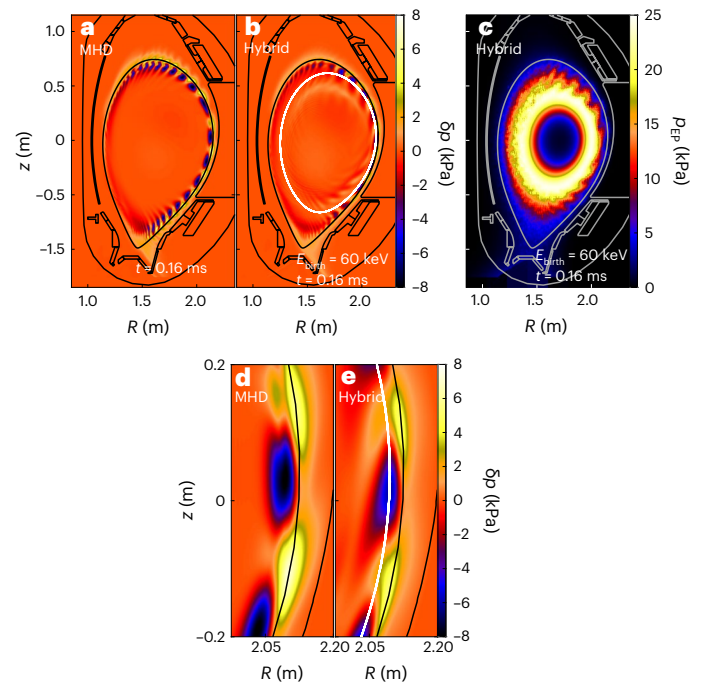


**Fig. 3 | Two-dimensional poloidal cross-sections.** **a, b**, Bulk plasma pressure perturbation ( $\delta p$ ) in a multi- $n$  MHD simulation at  $t = 0.16$  ms (**a**) and a multi- $n$  hybrid simulation with energetic particles with NBI energy  $E_{\text{birth}} = 60$  keV at  $t = 0.16$  ms (**b**). The white line shows the trajectory of a characteristic resonant energetic particle. **c**, Fast-ion pressure profile ( $p_{\text{ep}}$ ) for  $E_{\text{birth}} = 60$  keV at  $t = 0.16$  ms. **d, e**, Zooms of **a** (**d**) and **b** (**e**) at the plasma edge. In the figures,  $R$  and  $z$  correspond to the coordinates of the cylindrical coordinate system.

energy takes values notably larger compared with the MHD case. In Fig. 2a, the dashed line represents the energy of the  $n = 10$  mode ( $E_{n=10}$ ) for  $\rho_{\text{pol}} > 0.9$ . We have also performed multi- $n$  simulations (including  $n = 0, \dots, 10$  modes) to account for the nonlinear coupling of the modes. Figure 2b, c shows the time evolution of  $E_n$ ,  $n = 1, \dots, 10$ , for the MHD and hybrid simulations, respectively. The hybrid multi- $n$  simulation has been performed for  $E_{\text{birth}} = 60$  keV. In the multi- $n$  MHD simulation,  $n = 9$  and  $n = 10$  are the most unstable modes. However, in the hybrid simulation, although  $n = 10$  begins as the most unstable harmonic,  $n = 8$  becomes the most unstable mode in the nonlinear stage of the simulation with an energy almost five times larger than in the MHD simulation, indicating that the most unstable mode number is shifted to a lower one in the presence of fast-ion kinetic effects. Figure 2b, c also shows  $0.5 \times \sum_n E_n$ . In both the single- and multi- $n$  MHD simulations,  $E_{n=10}$  and  $\sum_n E_n$  take similar values, but in the hybrid simulations with  $E_{\text{birth}} = 60$  keV, the peak value of  $E_{n=10}$  is larger than that of  $\sum_n E_n$ . Notice that the mode energy obtained in the multi- $n$  simulations is divided by 10 because the mode energy is the volume integral of the mode energy density<sup>37</sup> and, as explained in Methods, the volume enclosed by the simulation domain in the single- $n$  simulations is ten times smaller than in the multi- $n$  simulations. Note that the dominant mode numbers simulated here are in the range of those observed during ELMs in AUG plasmas<sup>38</sup>. Figure 2d shows how the thermal plasma pressure gradient, fast ions, viscosity and nonlinear mode coupling contribute to  $E_{n=8}$  temporal evolution in the hybrid multi- $n$  simulation with  $E_{\text{birth}} = 60$  keV. Whereas the ELM is, as expected, triggered by the steep edge thermal plasma pressure gradient, the abrupt crash is dominated by a large energy exchange between the mode and fast ions. The nonlinear mode–mode coupling contribution to the drive and damping of the  $n = 8$  mode is included in Fig. 2d. This can be stabilizing or destabilizing depending on the relative phase of the different fluctuations’ terms. The nonlinear energy transfer plays a role in the evolution of high- $n$  modes, as its

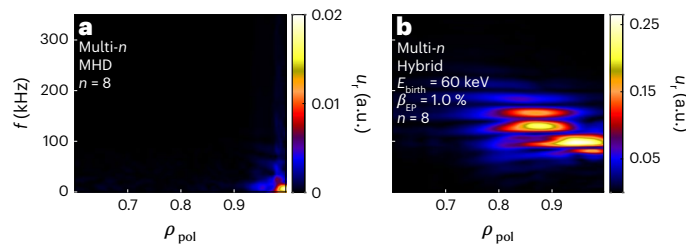


**Fig. 4 | Spatial frequency ELM profile. a, b,** Spectrograms of the radial velocity ( $u_r$ ) of  $n = 8$  mode in the MHD (a) and hybrid (b) multi- $n$  simulations in the radial coordinate ( $\rho_{pol}$ ) and frequency ( $f$ ) plane. The hybrid simulation shown in b considers the NBI energy  $E_{birth} = 60$  keV and  $\beta_{EP} = 1.0\%$ , where  $\beta_{EP}$  is the ratio between fast-ion pressure peak and magnetic pressure.

contribution is comparable to those coming from the thermal plasma pressure gradient, power exchange with fast ions and viscosity.

The spatial structure of the thermal plasma pressure perturbation is shown in a poloidal plane in Fig. 3 at a time with the maximum perturbation amplitude, for a MHD simulation (Fig. 3a) and a hybrid simulation with  $E_{birth} = 60$  keV (Fig. 3b), both for the multi- $n$  simulations. In the presence of energetic ion kinetic effects, the perturbation structure is radially extended to inner regions and strongly sheared. The radially extended ballooning structure causes a considerable fast-ion redistribution over a large plasma radius. This is observed in Fig. 3c, which shows the fast-ion pressure profile on a poloidal plane at the same timepoint as shown in Fig. 3b. The poloidal structure of the fast-ion pressure resembles the ballooning structure of the ELM with fingers in the energetic particle pressure extending into the far scrape-off layer.

The impact of the fast-ion kinetic effects on the spatial frequency pattern of the ELM crash is investigated in Fig. 4, which shows the spectrograms of  $n = 8$  radial velocity in the multi- $n$  MHD and hybrid simulations. Whereas in the MHD simulation the mode frequency takes rather low values (<20 kHz), in hybrid simulations, and during the nonlinear phase, the mode takes frequencies up to 200 kHz. In the presence of energetic ions, the mode becomes radially broad, as shown in Fig. 4b. The boost in frequency observed in the hybrid simulations is due to the imbalance of forces that appear in the MHD momentum equation. Our analysis reveals that the imbalance between the MHD and energetic particle forces,  $-\nabla p + \mathbf{j} \times \mathbf{B}$  and  $-\mathbf{j}_h \times \mathbf{B}$ , respectively, is the main reason for the boost of frequency observed in the hybrid kinetic-MHD simulations. Likewise, the ELM radial broadening in the presence of fast ions is dominated by their drive (Supplementary Fig. 1).

### Interaction mechanism between ELMs and energetic particles

To understand the interaction between ELMs and fast ions, Fig. 5 shows the power transfer between the ELM and the energetic particles for  $E_{birth} = 60$  keV at  $t = 0.16$  ms, when  $E_{n=8}$  is largest in the hybrid multi- $n$  simulation. The power transfer is given by<sup>39</sup>

$$P_h(\mathbf{x}, \mathbf{v}) = \sum_l w_l \frac{dE_l}{dt} S(\mathbf{x} - \mathbf{x}_l, \mathbf{v} - \mathbf{v}_l), \quad (1)$$

where  $w_l = V_l \delta f_l$  is the weight of the  $l$ th particle,  $V_l$  is the phase-space volume,  $\delta f_l$  is the fast-ion distribution perturbation,  $\frac{dE_l}{dt}$  is the time derivative of the kinetic energy of the  $l$ th particle and  $S$  is a shape function that allows to select particles with  $\mathbf{x}$  and  $\mathbf{v}$  coordinates in the phase space. Since  $P_h < 0$  at  $t = 0.16$  ms, the ELM is extracting energy from the fast ions.

The nature of the interaction between ELMs and fast ions shown here has been investigated by computing the possible wave-particle resonances for the energetic particle phase-space volumes with the

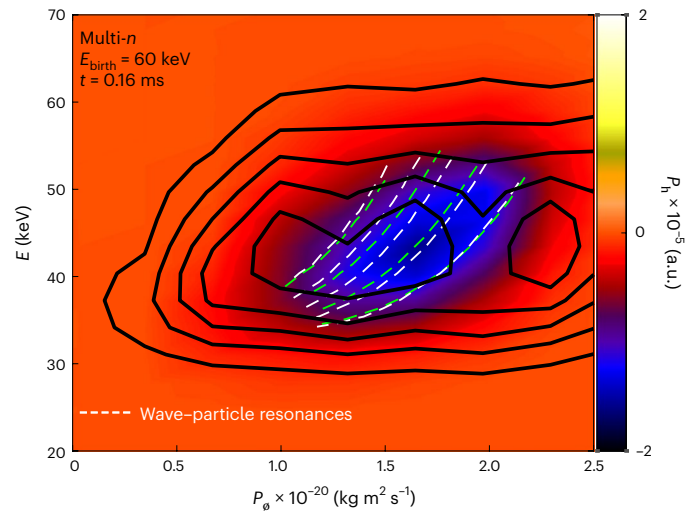


**Fig. 5 | Wave-particle interaction mechanism.** Power transfer ( $P_h$ ) for the hybrid simulation with NBI energy  $E_{birth} = 60$  keV at  $t = 0.16$  ms, when  $E_{n=8}$  is largest in the hybrid multi- $n$  simulation. The dashed white and green lines denote the resonance conditions with  $n = 10$  [ $p = (-9, -13)$ ] and  $n = 8$  [ $p = (-7, -10)$ ], respectively, for  $\mu = 1.6 \times 10^{-15} \text{ T}^{-1}$  ( $\mu$  is the magnetic moment of the particles). The black contours represent the fast-ion distribution.  $E$  and  $P_\phi$  denote the particle energy and toroidal canonical momentum coordinates, respectively.

largest power exchange from Fig. 5. The resonance condition between the energetic particle drift orbits and a wave is given by<sup>40,41</sup>

$$\omega_n - n\omega_\phi - p\omega_\theta \approx 0, \quad (2)$$

where  $\omega_n$  is the frequency of the mode at the corresponding timepoint,  $\omega_\phi$  and  $\omega_\theta$  are the toroidal and poloidal particle orbital frequencies, respectively, and  $p$  is the bounce harmonic. The dashed lines shown in Fig. 5 represent the resonance conditions for the main bounce harmonics with  $n = 10$  (white) and  $n = 8$  (green) and for a given magnetic moment  $\mu$ . The alignment of the power exchange structures with wave-particle resonances present in the plasma indicates that the wave-particle interaction observed here is likely to be mostly resonant. In fact, the orbital frequencies,  $\omega_\phi$  and  $\omega_\theta$ , for the energetic particles at the edge of the AUG plasma lie, mostly, within the range of frequencies observed in experimental magnetic and FILD spectrograms during ELM crashes. The trajectory of a typical resonant (passing) orbit with the ELM studied here is overlotted in white in Fig. 3b. The resulting power transfer observed in Fig. 5 is probably affected by a resonance overlap between the different modes considered in the simulation, given the closeness of the resonances.

The hybrid multi- $n$  simulations presented here reproduce some outstanding experimental observations such as the ELM spatio-temporal structure, the filamentary and frequency pattern of the measured fast-ion losses and the temporal evolution of the measured thermal particle losses during the entire ELM crash. Figure 6 shows the synthetic signals of a magnetic pick-up coil, a FILD system and a thermal particle loss detector developed in MEGA for comparisons with the experimental observations shown in Fig. 1. The synthetic magnetic spectrogram shown in Fig. 6a qualitatively reproduces the overall frequency pattern shown in Fig. 1a with a large frequency band up to -200–250 kHz dominating the crash at  $t \approx 0.16$  ms and with rather lower frequencies during the pre- and post-ELM crash. Similarly, the FILD spectrogram shown in Fig. 6b is dominated by a large frequency band up to -200–250 kHz that decays in amplitude and frequency right after the crash to frequencies below 100 kHz. The temporal evolution of the synthetic FILD signal depicted in Fig. 6c shows several fast-ion filaments during the ELM crash, similar to the experiment (Fig. 1c).

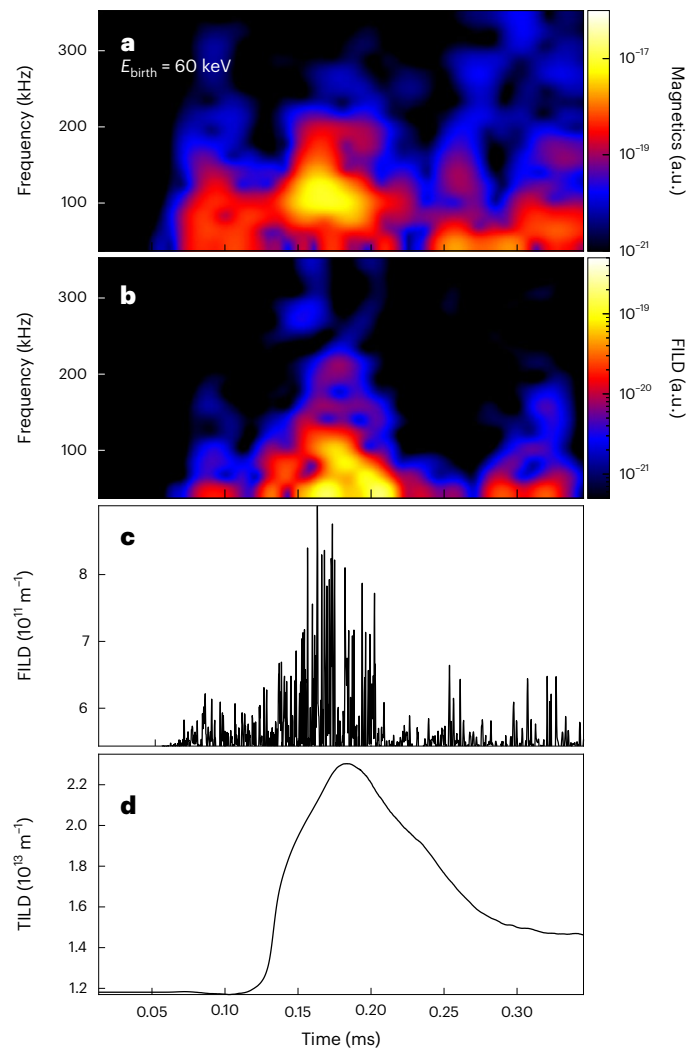


**Fig. 6 | Synthetic diagnostics for the multi- $n$  hybrid kinetic-MHD simulation.** **a, b**, Spectrograms of radial magnetic field fluctuations ( $\partial B_r/\partial t$ ) (**a**) and fast-ion losses (**b**) measured at the low field side (LFS) midplane measured by a synthetic FILD. **c**, The temporal evolution of the measured ELM-induced fast-ion losses. **d**, The temporal evolution of thermal particle losses to the outer divertor measured by a synthetic thermal ion loss detector (TILD). In **a–d**, the NBI energy is  $E_{\text{birth}} = 60$  keV.

In contrast to the filamentary structures observed in the temporal evolution of the fast-ion losses, the synthetic signal of the thermal ion losses at the outer divertor shows a single well-defined peak extended over the entire ELM crash as in the experimental observation (Fig. 6d). The synthetic thermal ion losses are obtained by integrating the bulk plasma density over a small surface near the outer divertor, as the thermo-currents shown in Fig. 1 are measured at the outer divertor. Comparing the divertor current signal in Fig. 1d with the synthetic thermal ion losses in Fig. 6d, we note that the MHD model is accurate enough to describe the evolution of the divertor current. Note that the simulated ELM duration is one order of magnitude smaller than that observed experimentally. This is in accordance with the resistivity value used for these simulations,  $\eta = 20 \times \eta_{\text{Spitzer}}$  (Supplementary Fig. 2 and ref. 42).

### Significance of the interaction between energetic particles and ELMs in ITER

To discuss the implications of these results for ITER, a preliminary estimation of an efficient resonant interaction between ELMs and fast

ions has been performed for representative energetic particle distributions and expected ELM parameters<sup>43</sup>. To this end, the Larmor radius  $\rho_L$  of fusion-born alpha particles and NBI ions has been compared with the expected edge ballooning mode wave number  $k_{\perp} \approx \frac{nq}{r}$  (ref. 44), with  $q$  being the safety factor and  $r$  the radial coordinate. If  $\rho_L k_{\perp} < 1$ , a substantial interaction between the mode and fast ions is expected<sup>26</sup>. For the standard H-mode of ITER, it is observed that  $\rho_L k_{\perp} < 1$  (with toroidal mode numbers  $n = 3, \dots, 10$ ) for both NBI ions ( $E_{\text{birth}} = 1$  MeV) and alpha particles. The mode numbers examined here are in the range of those expected during ELMs in ITER if they are not mitigated<sup>45</sup>. For the same particles and mode numbers, the drift orbit resonance condition is satisfied for a broad range of bounce harmonics  $p$ . This indicates that a considerable, and even stronger than in present machines, interaction between ELMs and energetic particles is expected in ITER. Whereas the majority of the NBI ions in ITER are born near the separatrix, thus suggesting a strong interaction with ELMs, most fusion-born alpha particles are born on-axis, suggesting a weak interaction with edge perturbations. A strong on-axis peaked alpha particle distribution is expected to trigger a broad spectrum of energetic particle-driven instabilities that will lead to a large alpha particle transport over the entire plasma radius<sup>46–50</sup>. Such a transported alpha particle population might interact with unabated ELMs in ITER.

### Online content

Any methods, additional references, Nature Portfolio reporting summaries, source data, extended data, supplementary information, acknowledgements, peer review information; details of author contributions and competing interests; and statements of data and code availability are available at <https://doi.org/10.1038/s41567-024-02715-6>.

### References

- Wagner, F. et al. Regime of improved confinement and high beta in neutral-beam-heated divertor discharges of the ASDEX tokamak. *Phys. Rev. Lett.* **49**, 1408–1412 (1982).
- Zohm, H. Edge localized modes (ELMs). *Plasma Phys. Control. Fusion* **38**, 105–128 (1996).
- Loarte, A. Chaos cuts ELMs down to size. *Nat. Phys.* **2**, 369–370 (2006).
- Evans, T. E. et al. Edge stability and transport control with resonant magnetic perturbations in collisionless tokamak plasmas. *Nat. Phys.* **2**, 419–423 (2006).
- Li, J. et al. A long-pulse high-confinement plasma regime in the Experimental Advanced Superconducting Tokamak. *Nat. Phys.* **9**, 817–821 (2013).
- Park, J. K. et al. 3D field phase-space control in tokamak plasmas. *Nat. Phys.* **14**, 1223–1228 (2018).
- Ham, C. et al. Filamentary plasma eruptions and their control on the route to fusion energy. *Nat. Rev. Phys.* **2**, 159–167 (2020).
- Yang, S. et al. Tailoring tokamak error fields to control plasma instabilities and transport. *Nat. Commun.* **15**, 1275 (2024).
- Kim, S. K. et al. Highest fusion performance without harmful edge energy bursts in tokamak. *Nat. Commun.* **15**, 3990 (2024).
- Ding, S. et al. A high-density and high-confinement tokamak plasma regime for fusion energy. *Nature* **629**, 555–560 (2024).
- Connor, J. W. et al. Magnetohydrodynamic stability of tokamak edge plasmas. *Phys. Plasmas* **5**, 2687–2700 (1998).
- Wilson, H. R. et al. Ideal magnetohydrodynamic stability of the tokamak high-confinement-mode edge region. *Phys. Plasmas* **6**, 1925–1934 (1999).
- Snyder, P. B. et al. Edge localized modes and the pedestal: a model based on coupled peeling–ballooning modes. *Phys. Plasmas* **9**, 2037–2043 (2002).
- Snyder, P. B. et al. ELMs and constraints on the H-mode pedestal: peeling–ballooning stability calculation and comparison with experiment. *Nucl. Fusion* **44**, 320–328 (2004).

15. Orain, F. et al. Resistive reduced MHD modeling of multi-edge-localized-mode cycles in tokamak X-point plasmas. *Phys. Rev. Lett.* **114**, 035001 (2015).
16. Pamela, S. J. P. et al. Resistive MHD simulation of edge-localized-modes for double-null discharges in the MAST device. *Plasma Phys. Control. Fusion* **55**, 095001 (2013).
17. Liu, Z. X. et al. Three dimensional nonlinear simulations of edge localized modes on the EAST tokamak using BOUT++ code. *Phys. Plasmas* **21**, 090705 (2014).
18. Brennan, D. P. et al. Computing nonlinear magnetohydrodynamic edge localized instabilities in fusion plasmas. *J. Phys. Conf. Ser.* **46**, 63–72 (2006).
19. Diu, X. Q. et al. Nonlinear simulations of peeling–ballooning modes with anomalous electron viscosity and their role in edge localized mode crashes. *Phys. Rev. Lett.* **105**, 175005 (2010).
20. Pace, D. et al. Keeping fusion plasmas hot. *Physics Today* **68**, 34–39 (2015).
21. Mazzi, S. et al. Enhanced performance in fusion plasmas through turbulence suppression by megaelectronvolt ions. *Nat. Phys.* **18**, 776–782 (2022).
22. Han, H. et al. A sustained high-temperature fusion plasma regime facilitated by fast ions. *Nature* **609**, 269–275 (2022).
23. Garcia-Munoz, M. et al. MHD induced fast-ion losses on ASDEX Upgrade. *Nucl. Fusion* **49**, 085014 (2009).
24. Graves, J. P. et al. Control of magnetohydrodynamic stability by phase space engineering of energetic ions in tokamak plasmas. *Nat. Commun.* **3**, 624 (2012).
25. Kazakov, Y. O. et al. Efficient generation of energetic ions in multi-ion plasmas by radio-frequency heating. *Nat. Phys.* **13**, 973–978 (2017).
26. Heidbrink, W. W. et al. Mechanisms of energetic-particle transport in magnetically confined plasmas. *Phys. Plasmas* **27**, 030901 (2020).
27. Bierwage, A. et al. Energy-selective confinement of fusion-born alpha particles during internal relaxations in a tokamak plasma. *Nat. Commun.* **13**, 3941 (2022).
28. Garcia-Munoz, M. et al. Fast-ion redistribution and loss due to edge perturbations in the ASDEX Upgrade, DIII-D and KSTAR tokamaks. *Nucl. Fusion* **53**, 123008 (2013).
29. Garcia-Munoz, M. et al. Scintillator based detector for fast-ion losses induced by magnetohydrodynamic instabilities in the ASDEX upgrade tokamak. *Rev. Sci. Instrum.* **80**, 053503 (2009).
30. Galdon-Quiroga, J. et al. Beam-ion acceleration during edge localized modes in the ASDEX Upgrade tokamak. *Phys. Rev. Lett.* **121**, 025002 (2018).
31. Gil, L. et al. Stationary ELM-free H-mode in ASDEX Upgrade. *Nucl. Fusion* **60**, 054003 (2020).
32. Wolfrum, E. et al. Characterization of edge profiles and fluctuations in discharges with type-II and nitrogen-mitigated edge localized modes in ASDEX Upgrade. *Plasma Phys. Control. Fusion* **53**, 085026 (2011).
33. Harrer, G. F. et al. Parameter dependences of small edge localized modes (ELMs). *Nucl. Fusion* **58**, 112001 (2018).
34. Todo, Y. et al. Linear and nonlinear particle-magnetohydrodynamic simulations of the toroidal Alfvén eigenmode. *Phys. Plasmas* **5**, 1321–1327 (1998).
35. Mink, A. F. et al. Nonlinear coupling induced toroidal structure of edge localized modes. *Nucl. Fusion* **58**, 026011 (2018).
36. Laggner, F. M. et al. Inter-ELM pedestal localized fluctuations in tokamaks: summary of multi-machine observations. *Nucl. Mater. Energy* **19**, 479–486 (2019).
37. Todo, Y. et al. Nonlinear magnetohydrodynamic effects on Alfvén eigenmode evolution and zonal flow generation. *Nucl. Fusion* **50**, 084016 (2010).
38. Mink, F. et al. Toroidal mode number determination of ELM associated phenomena on ASDEX Upgrade. *Plasma Phys. Control. Fusion* **58**, 125013 (2016).
39. Bierwage, A. Mechanisms for rapid chirping and convective amplification. *Phys. Plasmas* **23**, 042512 (2016).
40. White, R. B. et al. Theory of mode-induced beam particle loss in tokamaks. *Phys. Fluids* **26**, 2958–2965 (1983).
41. Chen, L. & Zonca, F. Physics of Alfvén waves and energetic particles in burning plasmas. *Rev. Mod. Phys.* **88**, 015008 (2016).
42. Pamela, S. J. P. et al. Non-linear MHD simulations of ELMs in JET and quantitative comparisons to experiments. *Plasma Phys. Control. Fusion* **58**, 014026 (2016).
43. Sips, A. C. C. et al. Advanced scenarios for ITER operation. *Plasma Phys. Control. Fusion* **47**, A19–A40 (2005).
44. Morales, J. A. et al. Edge localized mode rotation and the nonlinear dynamics of filaments. *Phys. Plasmas* **23**, 042513 (2016).
45. Becoulet, M. et al. Non-linear MHD modelling of edge localized modes suppression by resonant magnetic perturbations in ITER. *Nucl. Fusion* **62**, 066022 (2022).
46. Todo, Y. et al. Large-scale simulation of energetic particle driven magnetohydrodynamic instabilities in ITER plasmas. *Plasma Fus. Res.* **9**, 3403068 (2014).
47. Lauber, P. Local and global kinetic stability analysis of Alfvén eigenmodes in the 15 MA ITER scenario. *Plasma Phys. Control. Fusion* **57**, 054011 (2015).
48. Pinches, S. D. et al. Energetic ions in ITER plasmas. *Phys. Plasmas* **22**, 021807 (2015).
49. Schneller, M. et al. Nonlinear energetic particle transport in the presence of multiple Alfvén waves in ITER. *Plasma Phys. Control. Fusion* **58**, 014019 (2016).
50. Hayward-Schneider, T. et al. Global linear and nonlinear gyrokinetic modelling of Alfvén eigenmodes in ITER. *Nucl. Fusion* **61**, 036045 (2021).

**Publisher's note** Springer Nature remains neutral with regard to jurisdictional claims in published maps and institutional affiliations.

**Open Access** This article is licensed under a Creative Commons Attribution 4.0 International License, which permits use, sharing, adaptation, distribution and reproduction in any medium or format, as long as you give appropriate credit to the original author(s) and the source, provide a link to the Creative Commons licence, and indicate if changes were made. The images or other third party material in this article are included in the article's Creative Commons licence, unless indicated otherwise in a credit line to the material. If material is not included in the article's Creative Commons licence and your intended use is not permitted by statutory regulation or exceeds the permitted use, you will need to obtain permission directly from the copyright holder. To view a copy of this licence, visit <http://creativecommons.org/licenses/by/4.0/>.

© The Author(s) 2025

<sup>1</sup>University of Seville, Seville, Spain. <sup>2</sup>Universitat Politècnica de Catalunya, Barcelona, Spain. <sup>3</sup>University of California at Irvine, Irvine, CA, USA.

<sup>4</sup>National Institute for Fusion Science, Toki, Japan. <sup>5</sup>Graduate School of Advanced Science and Engineering, Hiroshima University, Higashi-Hiroshima, Japan. <sup>6</sup>Aalto University, Espoo, Finland. <sup>7</sup>Culham Center for Fusion Energy, Abingdon, UK. <sup>86</sup>Present address: Ecole Polytechnique Fédérale de Lausanne, Swiss Plasma Center, Lausanne, Switzerland. <sup>87</sup>Present address: University of Seville, Seville, Spain. <sup>88</sup>Present address: Southwestern Institute of Physics, Chengdu, China. \*Lists of authors and their affiliations appear at the end of the paper. ✉e-mail: [jdominguezpalacios@us.es](mailto:jdominguezpalacios@us.es); [mgm@us.es](mailto:mgm@us.es)

## the ASDEX Upgrade Team

E. Alessi<sup>8</sup>, C. Angioni<sup>9</sup>, N. Arden<sup>9</sup>, V. Artigues<sup>9</sup>, M. Astrain Etxezarreta<sup>9</sup>, O. Asunta<sup>10</sup>, M. Balden<sup>9</sup>, V. Bandaru<sup>9</sup>, A. Banon Navarro<sup>9</sup>, M. Bauer<sup>9</sup>, A. Bergmann<sup>9</sup>, M. Bergmann<sup>9</sup>, J. Bernardo<sup>11</sup>, M. Bernert<sup>9</sup>, A. Biancalani<sup>12</sup>, R. Bielajew<sup>13</sup>, R. Bilato<sup>9</sup>, G. Birkenmeier<sup>9,14</sup>, T. Blanken<sup>15</sup>, V. Bobkov<sup>9</sup>, A. Bock<sup>9</sup>, L. Bock<sup>9</sup>, T. Body<sup>9</sup>, T. Bolzonella<sup>16</sup>, N. Bonanomi<sup>9</sup>, A. Bortolon<sup>17</sup>, B. Böswirth<sup>9</sup>, C. Bottereau<sup>18</sup>, A. Bottino<sup>9</sup>, H. van den Brand<sup>15</sup>, M. Brenzke<sup>19</sup>, S. Brezinsek<sup>19</sup>, D. Brida<sup>9</sup>, F. Brochard<sup>20</sup>, J. Buchanan<sup>21</sup>, A. Buhler<sup>9</sup>, A. Burckhart<sup>9</sup>, Y. Camenen<sup>22</sup>, B. Cannas<sup>23</sup>, P. Cano Megas<sup>9</sup>, D. Carlton<sup>9</sup>, M. Carr<sup>21</sup>, P. Carvalho<sup>11</sup>, C. Castaldo<sup>24</sup>, A. Castillo Castillo<sup>9</sup>, A. Cathey<sup>9</sup>, M. Cavedon<sup>25</sup>, C. Cazzaniga<sup>16</sup>, C. Challis<sup>21</sup>, A. Chan Kin<sup>9</sup>, A. Chomiczewska<sup>26</sup>, C. Cianfarani<sup>24</sup>, F. Clairet<sup>18</sup>, S. Coda<sup>27</sup>, R. Coelho<sup>11</sup>, J. W. Coenen<sup>19</sup>, L. Colas<sup>18</sup>, G. Conway<sup>9</sup>, S. Costea<sup>28</sup>, D. Coster<sup>9</sup>, T. Cote<sup>29</sup>, A. J. Creely<sup>13</sup>, G. Croci<sup>8</sup>, D. J. Cruz Zabala<sup>1</sup>, G. Cseh<sup>30</sup>, I. Cziegler<sup>31</sup>, O. D'Arcangelo<sup>32</sup>, A. Dal Molin<sup>25</sup>, P. David<sup>9</sup>, C. Day<sup>33</sup>, M. de Baar<sup>15</sup>, P. de Marné<sup>9</sup>, R. Delogu<sup>16</sup>, P. Denner<sup>19</sup>, A. Di Siena<sup>9</sup>, M. Dibon<sup>9</sup>, J. J. Dominguez-Palacios Durán<sup>1</sup>, D. Dunai<sup>30</sup>, M. Dreval<sup>34</sup>, M. Dunne<sup>9</sup>, B. P. Duval<sup>27</sup>, R. Dux<sup>9</sup>, T. Eich<sup>9</sup>, S. Elgeti<sup>9</sup>, A. Encheva<sup>35</sup>, B. Esposito<sup>24</sup>, E. Fable<sup>9</sup>, M. Faitsch<sup>9</sup>, D. Fajardo Jimenez<sup>9</sup>, U. Fantz<sup>9</sup>, M. Farnik<sup>36</sup>, H. Faugel<sup>9</sup>, F. Felici<sup>27</sup>, O. Ficker<sup>36</sup>, A. Figueredo<sup>11</sup>, R. Fischer<sup>9</sup>, O. Ford<sup>37</sup>, L. Frassinetti<sup>38</sup>, M. Fröschle<sup>9</sup>, G. Fuchert<sup>37</sup>, J. C. Fuchs<sup>9</sup>, H. Fünfgelder<sup>9</sup>, S. Futatani<sup>39</sup>, K. Galazka<sup>26</sup>, J. Galdon-Quiroga<sup>1</sup>, D. Gallart Escolà<sup>39</sup>, A. Gallo<sup>18</sup>, Y. Gao<sup>19</sup>, S. Garavaglia<sup>8</sup>, M. Garcia-Munoz<sup>1</sup>, B. Geiger<sup>29</sup>, L. Giannone<sup>9</sup>, S. Gibson<sup>40</sup>, L. Gil<sup>11</sup>, E. Giovannozzi<sup>24</sup>, I. Girka<sup>9</sup>, O. Girka<sup>9</sup>, T. Gleiter<sup>9</sup>, S. Glöggl<sup>9,14</sup>, M. Gobbin<sup>16</sup>, J. C. Gonzalez<sup>9</sup>, J. Gonzalez-Martin<sup>1,3,87</sup>, T. Goodman<sup>27</sup>, G. Gorini<sup>25</sup>, T. Görler<sup>9</sup>, D. Gradic<sup>37</sup>, G. Granucci<sup>8</sup>, A. Gräter<sup>9</sup>, G. Grenfell<sup>9</sup>, H. Greuner<sup>9</sup>, M. Griener<sup>9</sup>, M. Groth<sup>10</sup>, O. Grover<sup>9</sup>, A. Gude<sup>9</sup>, L. Guimaraes<sup>11</sup>, S. Günter<sup>9</sup>, D. Hachmeister<sup>11</sup>, A. H. Hakola<sup>41</sup>, C. Ham<sup>21</sup>, T. Happel<sup>9</sup>, N. den Harder<sup>9</sup>, G. Harrer<sup>42</sup>, J. Harrison<sup>21</sup>, V. Hauer<sup>33</sup>, T. Hayward-Schneider<sup>9</sup>, B. Heinemann<sup>9</sup>, P. Heinrich<sup>9</sup>, T. Hellsten<sup>43</sup>, S. Henderson<sup>21</sup>, P. Hennequin<sup>44</sup>, M. Herschel<sup>9</sup>, S. Heuraux<sup>20</sup>, A. Herrmann<sup>9</sup>, E. Heyn<sup>45</sup>, F. Hitzler<sup>9,14</sup>, J. Hobirk<sup>9</sup>, K. Höfler<sup>37</sup>, S. Hörmann<sup>9</sup>, J. H. Holm<sup>46</sup>, M. Hölzl<sup>9</sup>, C. Hopf<sup>9</sup>, L. Horvath<sup>31</sup>, T. Höschen<sup>9</sup>, A. Houben<sup>20</sup>, A. Hubbard<sup>13</sup>, A. Huber<sup>19</sup>, K. Hunger<sup>9</sup>, V. Igochine<sup>9</sup>, M. Iliasova<sup>47</sup>, J. Illerhaus<sup>9</sup>, K. Insulander Björk<sup>48</sup>, C. Ionita-Schrittwieser<sup>28</sup>, I. Ivanova-Stanik<sup>26</sup>, W. Jacob<sup>9</sup>, N. Jaksic<sup>9</sup>, A. Jansen van Vuuren<sup>1,86</sup>, F. Jaulmes<sup>36</sup>, F. Jenko<sup>9</sup>, T. Jensen<sup>46</sup>, E. Joffrin<sup>18</sup>, A. Kallenbach<sup>9</sup>, J. Kalis<sup>9</sup>, A. Kappatou<sup>9</sup>, J. Karhunen<sup>10</sup>, C.-P. Käsemann<sup>9</sup>, S. Kasilov<sup>45,49</sup>, Y. Kazakov<sup>50</sup>, A. Kendl<sup>28</sup>, W. Kernbichler<sup>42</sup>, E. Khilkevitch<sup>47</sup>, M. Kircher<sup>9</sup>, A. Kirk<sup>21</sup>, S. Kjer Hansen<sup>13</sup>, V. Klevarova<sup>51</sup>, F. Klosek<sup>9</sup>, G. Kocsis<sup>30</sup>, M. Koleva<sup>9</sup>, M. Komm<sup>36</sup>, M. Kong<sup>27</sup>, A. Krämer-Flecken<sup>19</sup>, M. Krause<sup>9</sup>, I. Krebs<sup>15</sup>, A. Kreuzeder<sup>9</sup>, K. Krieger<sup>9</sup>, O. Kudlacek<sup>9</sup>, D. Kulla<sup>37</sup>, T. Kurki-Suonio<sup>10</sup>, B. Kurzan<sup>9</sup>, B. Labit<sup>27</sup>, K. Lackner<sup>9</sup>, F. Laggner<sup>17</sup>, A. Lahtinen<sup>10</sup>, P. Lainer<sup>42</sup>, P. T. Lang<sup>9</sup>, P. Lauber<sup>9</sup>, L. Leppin<sup>9</sup>, E. Lerche<sup>9</sup>, N. Leuthold<sup>43</sup>, L. Li<sup>19</sup>, J. Likonon<sup>41</sup>, O. Linder<sup>9</sup>, H. Lindl<sup>9</sup>, B. Lipschultz<sup>31</sup>, Y. Liu<sup>43</sup>, Z. Lu<sup>9</sup>, T. Luda di Cortemiglia<sup>9</sup>, N. C. Luhmann<sup>52</sup>, T. Lunt<sup>9</sup>, A. Lysoivan<sup>50</sup>, T. Maceina<sup>9</sup>, J. Madsen<sup>46</sup>, A. Magnanimo<sup>9</sup>, H. Maier<sup>9</sup>, J. Mailloux<sup>21</sup>, R. Maingi<sup>17</sup>, O. Maj<sup>9</sup>, E. Maljaars<sup>15</sup>, V. Maquet<sup>50</sup>, A. Mancini<sup>8</sup>, A. Manhard<sup>9</sup>, P. Mantica<sup>8</sup>, M. Mantsinen<sup>39</sup>, P. Manz<sup>49</sup>, M. Maraschek<sup>9</sup>, C. Marchetto<sup>53</sup>, M. Markl<sup>42</sup>, L. Marrelli<sup>16</sup>, P. Martin<sup>16</sup>, F. Matos<sup>9</sup>, M. Mayer<sup>9</sup>, P. J. McCarthy<sup>54</sup>, R. McDermott<sup>9</sup>, G. Meng<sup>9</sup>, R. Merkel<sup>9</sup>, A. Merle<sup>27</sup>, H. Meyer<sup>21</sup>, M. Michelin<sup>9</sup>, D. Milanesio<sup>53</sup>, V. Mitterauer<sup>9</sup>, P. Molina Cabrera<sup>9</sup>, M. Muraca<sup>9</sup>, F. Nabais<sup>11</sup>, V. Naulin<sup>46</sup>, R. Nazikian<sup>17</sup>, R. D. Nem<sup>46</sup>, R. Neu<sup>9,55</sup>, A. H. Nielsen<sup>46</sup>, S. K. Nielsen<sup>46</sup>, T. Nishizawa<sup>9</sup>, M. Nocente<sup>25</sup>, I. Novikau<sup>9</sup>, S. Nowak<sup>8</sup>, R. Ochoukov<sup>9</sup>, J. Olsen<sup>46</sup>, P. Oyola<sup>1</sup>, O. Pan<sup>9</sup>, G. Papp<sup>9</sup>, A. Pau<sup>27</sup>, G. Pautasso<sup>9</sup>, C. Paz-Soldan<sup>43</sup>, M. Peglau<sup>9</sup>, E. Peluso<sup>56</sup>, P. Petersson<sup>38</sup>, C. Piron<sup>16</sup>, U. Plank<sup>9</sup>, B. Plaum<sup>57</sup>, B. Plöckl<sup>9</sup>, V. Plyusnin<sup>11</sup>, G. Pokol<sup>30,58</sup>, E. Poli<sup>9</sup>, A. Popa<sup>9</sup>, L. Porte<sup>27</sup>, J. Puchmayr<sup>9</sup>, T. Pütterich<sup>9</sup>, L. Radovanovic<sup>42</sup>, M. Ramisch<sup>57</sup>, J. Rasmussen<sup>46</sup>, G. Ratta<sup>59</sup>, S. Ratynskaia<sup>38</sup>, G. Raupp<sup>9</sup>, A. Redl<sup>60</sup>, D. Réfy<sup>30</sup>, M. Reich<sup>9</sup>, F. Reimold<sup>37</sup>, D. Reiser<sup>19</sup>, M. Reisner<sup>9</sup>, D. Reiter<sup>19</sup>, B. Rettino<sup>9</sup>, T. Ribeiro<sup>9</sup>, D. Ricci<sup>8</sup>, R. Riedl<sup>9</sup>, J. Riesch<sup>9</sup>, J. F. Rivero Rodriguez<sup>1</sup>, G. Rocchi<sup>24</sup>, P. Rodriguez-Fernandez<sup>13</sup>, V. Rohde<sup>9</sup>, G. Ronchi<sup>15</sup>, M. Rott<sup>9</sup>, M. Rubel<sup>38</sup>, D. A. Ryan<sup>21</sup>, F. Ryter<sup>9</sup>, S. Saarelma<sup>21</sup>, M. Salewski<sup>46</sup>, A. Salmi<sup>10</sup>, O. Samoylov<sup>9</sup>, L. Sanchis Sanchez<sup>6,87</sup>, J. Santos<sup>11</sup>, O. Sauter<sup>27</sup>, G. Schall<sup>9</sup>, A. Schlüter<sup>9</sup>, J. Scholte<sup>15</sup>, K. Schmid<sup>9</sup>, O. Schmitz<sup>29</sup>, P. A. Schneider<sup>9</sup>, R. Schrittwieser<sup>28</sup>, M. Schubert<sup>9</sup>, C. Schuster<sup>9</sup>, N. Schwarz<sup>9</sup>, T. Schwarz-Selinger<sup>9</sup>, J. Schweinzer<sup>9</sup>, F. Sciortino<sup>9</sup>, O. Seibold-Benjak<sup>9</sup>, A. Shabbir<sup>51</sup>, A. Shalpegin<sup>27</sup>, S. Sharapov<sup>21</sup>, U. Sheikh<sup>27</sup>, A. Shevelev<sup>47</sup>, G. Sias<sup>23</sup>, M. Siccino<sup>9</sup>, B. Sieglin<sup>9</sup>, A. Sigalov<sup>9</sup>, A. Silva<sup>11</sup>, C. Silva<sup>11</sup>, D. Silvagni<sup>9</sup>, J. Simpson<sup>21</sup>, S. Sipilä<sup>10</sup>, A. Snicker<sup>10</sup>, E. Solano<sup>59</sup>, C. Sommariva<sup>27</sup>, C. Sozzi<sup>8</sup>, M. Spacek<sup>9</sup>, G. Spizzo<sup>16</sup>, M. Spolaore<sup>16</sup>, A. Stegmeir<sup>9</sup>, M. Stejner<sup>46</sup>, D. Stieglitz<sup>9</sup>, J. Stober<sup>9</sup>, U. Stroth<sup>9,14</sup>, E. Strumberger<sup>9</sup>, G. Suarez Lopez<sup>9</sup>, W. Suttrop<sup>9</sup>, T. Szepesi<sup>30</sup>, B. Tál<sup>9</sup>, T. Tala<sup>41</sup>, W. Tang<sup>9</sup>, G. Tardini<sup>9</sup>, M. Tardocchi<sup>8</sup>, D. Terranova<sup>16</sup>, M. Teschke<sup>9</sup>, E. Thorén<sup>38</sup>, W. Tierens<sup>9</sup>, D. Told<sup>9</sup>, W. Treutterer<sup>9</sup>, G. Trevisan<sup>16</sup>, M. Tripský<sup>50</sup>, P. Ulbl<sup>9</sup>, G. Urbanczyk<sup>9</sup>, M. Usoltseva<sup>9</sup>, M. Valisa<sup>16</sup>, M. Valovic<sup>21</sup>, M. van Zeeland<sup>43</sup>, F. Vannini<sup>9</sup>, B. Vanovac<sup>13</sup>, P. Varela<sup>11</sup>, S. Varoutis<sup>33</sup>, T. Verdier<sup>46</sup>, G. Verdoolaege<sup>41,43</sup>, N. Vianello<sup>16</sup>, J. Vicente<sup>11</sup>, T. Vierle<sup>9</sup>, E. Viezzer<sup>1</sup>, I. Voitsekhovitch<sup>21</sup>, U. von Toussaint<sup>9</sup>, D. Wagner<sup>9</sup>, X. Wang<sup>9</sup>, M. Weiland<sup>9</sup>, D. Wendler<sup>9,14</sup>, A. E. White<sup>13</sup>, M. Willensdorfer<sup>9</sup>, B. Wirlinger<sup>9</sup>, M. Wischmeier<sup>9</sup>, R. Wolf<sup>37</sup>, E. Wolfrum<sup>9</sup>, Q. Yang<sup>61</sup>, C. You<sup>13</sup>, Q. Yu<sup>9</sup>, R. Zagorski<sup>26</sup>, I. Zammuto<sup>9</sup>, T. Zehetbauer<sup>9</sup>, W. Zhang<sup>61</sup>, W. Zholobenko<sup>9</sup>, A. Zibrov<sup>9</sup>, M. Zilker<sup>9</sup>, C. F. B. Zimmermann<sup>9,14</sup>, A. Zito<sup>9</sup>, H. Zohm<sup>9</sup> & S. Zoletnik<sup>30</sup>

<sup>8</sup>ENE, IFP-CNR, Milan, Italy. <sup>9</sup>Max-Planck-Institute für Plasmaphysik, Garching, Germany. <sup>10</sup>Department of Applied Physics, Aalto University, Espoo, Finland. <sup>11</sup>Instituto de Plasmas e Fusão Nuclear, Instituto Superior Técnico, Universidade de Lisboa, Lisbon, Portugal. <sup>12</sup>Modeling Group, École supérieure d'ingénieurs Léonard-de-Vinci, Courbevoie, France. <sup>13</sup>MIT Plasma Science and Fusion Center, Cambridge, MA, USA. <sup>14</sup>Physik-Department E28, Technische

Universität München, Garching, Germany. <sup>15</sup>Eindhoven, University of Technology, Eindhoven, the Netherlands. <sup>16</sup>Consorzio RFX, Padua, Italy. <sup>17</sup>Princeton Plasma Physics Laboratory, Princeton, NJ, USA. <sup>18</sup>CEA/IRFM, Saint Paul Lez Durance, France. <sup>19</sup>Forschungszentrum Jülich, Jülich, Germany. <sup>20</sup>Institut Jean Lamour, Université de Lorraine, Nancy, France. <sup>21</sup>CCFE, Culham Science Centre, Abingdon, UK. <sup>22</sup>Aix-Marseille University, CNRS, Marseille, France. <sup>23</sup>Department of Electrical and Electronic Engineering, University of Cagliari, Cagliari, Italy. <sup>24</sup>ENEA, Centro Ricerche Frascati, Frascati RM, Italy. <sup>25</sup>ENEA, University of Milano-Bicocca, Milan, Italy. <sup>26</sup>Institute of Plasma Physics and Laser Microfusion, Warsaw, Poland. <sup>27</sup>Ecole Polytechnique Fédérale de Lausanne, Swiss Plasma Center, Lausanne, Switzerland. <sup>28</sup>ÖAW, IAP, University of Innsbruck, Innsbruck, Austria. <sup>29</sup>University of Wisconsin, Madison, WI, USA. <sup>30</sup>Centre for Energy Research, Budapest, Hungary. <sup>31</sup>York Plasma Institute, University of York, York, UK. <sup>32</sup>ENEA Consorzio CREATE, Naples, Italy. <sup>33</sup>Karlsruhe Institut für Technologie, Karlsruhe, Germany. <sup>34</sup>Institute of Plasma Physics, National Science Center Kharkov Institute of Physics and Technology, Krakov, Ukraine. <sup>35</sup>ITER Organization, Saint-Paul-lez-Durance, France. <sup>36</sup>Institute of Plasma Physics of the CAS, Praha, Czech Republic. <sup>37</sup>Max-Planck-Institut für Plasmaphysik, Greifswald, Germany. <sup>38</sup>KTH Royal Institute of Technology, Stockholm, Sweden. <sup>39</sup>Barcelona Supercomputing Center, Barcelona, Spain. <sup>40</sup>Department of Physics, Durham University, Durham, UK. <sup>41</sup>VTT Technical Research Centre of Finland, Espoo, Finland. <sup>42</sup>ÖAW, IAP, Vienna University of Technology, Vienna, Austria. <sup>43</sup>General Atomics, San Diego, CA, USA. <sup>44</sup>Laboratoire de Physique des Plasmas, Ecole Polytechnique, Palaiseau, France. <sup>45</sup>ÖAW, Graz University of Technology, Graz, Austria. <sup>46</sup>Department of Physics, Technical University of Denmark, Lyngby, Denmark. <sup>47</sup>Ioffe Institute, St Petersburg, Russian Federation. <sup>48</sup>Department of Physics, Chalmers University of Technology, Gothenburg, Sweden. <sup>49</sup>Universität Greifswald, Greifswald, Germany. <sup>50</sup>ERM/KMS, Brussels, Belgium. <sup>51</sup>Ghent University, Ghent, Belgium. <sup>52</sup>Department of Electrical and Computer Engineering, University of California, Davis, Davis, CA, USA. <sup>53</sup>ISC-CNR and Politecnico di Torino, Turin, Italy. <sup>54</sup>Department of Physics, National University of Ireland, Cork, Ireland. <sup>55</sup>Technische Universität München, Garching, Germany. <sup>56</sup>Department of Industrial Engineering, University of Rome, Rome, Italy. <sup>57</sup>IGVP Universität Stuttgart, Stuttgart, Germany. <sup>58</sup>Budapest University of Technology and Economics, Budapest, Hungary. <sup>59</sup>Laboratorio Nacional de Fusión, CIEMAT, Madrid, Spain. <sup>60</sup>DEIM Department, Università degli Studi della Tuscia, Viterbo, Italy. <sup>61</sup>Chinese Academy of Sciences, Hefei, China.

### the EuroFUSION MST1 Team

**B. Labit<sup>27</sup>, T. Eich<sup>9</sup>, G. F. Harrer<sup>42</sup>, E. Wolfrum<sup>9</sup>, M. Bernert<sup>9</sup>, M. G. Dunne<sup>9</sup>, L. Frassinetti<sup>38</sup>, P. Hennequin<sup>44</sup>, R. Maurizio<sup>27</sup>, A. Merle<sup>27</sup>, H. Meyer<sup>7</sup>, S. Saarela<sup>7</sup>, U. Sheikh<sup>27</sup>, J. Adamek<sup>36</sup>, M. Agostini<sup>16</sup>, D. Aguiam<sup>11</sup>, R. Akers<sup>7</sup>, R. Albanese<sup>62</sup>, C. Albert<sup>45</sup>, E. Alessi<sup>8</sup>, R. Ambrosino<sup>63</sup>, Y. Andrébe<sup>27</sup>, C. Angioni<sup>9</sup>, G. Apruzzese<sup>24</sup>, M. Aradi<sup>45</sup>, H. Arnichand<sup>27</sup>, F. Auremma<sup>16</sup>, G. Avdeeva<sup>46</sup>, J. M. Ayllon-Guerola<sup>1</sup>, F. Bagnato<sup>27</sup>, V. K. Bandaru<sup>9</sup>, M. Barnes<sup>7,64</sup>, L. Barrera-Orte<sup>65</sup>, P. Bettini<sup>16</sup>, R. Bilato<sup>9</sup>, O. Biletskyi<sup>34</sup>, P. Bilkova<sup>36</sup>, W. Bin<sup>8</sup>, P. Blanchard<sup>27</sup>, T. Blanken<sup>15</sup>, V. Bobkov<sup>9</sup>, A. Bock<sup>9</sup>, D. Boeyaert<sup>19</sup>, K. Bogar<sup>36</sup>, O. Bogar<sup>36</sup>, P. Bohm<sup>36</sup>, T. Bolzonella<sup>16</sup>, F. Bombarda<sup>24</sup>, L. Boncagni<sup>24</sup>, F. Bouquey<sup>18</sup>, C. Bowman<sup>31</sup>, S. Brezinsek<sup>19</sup>, D. Brida<sup>9</sup>, D. Brunetti<sup>8</sup>, J. Bucalossi<sup>18</sup>, J. Buchanan<sup>7</sup>, J. Buermans<sup>50</sup>, H. Bufferand<sup>18</sup>, S. Buller<sup>51</sup>, P. Buratti<sup>24</sup>, A. Burckhart<sup>9</sup>, G. Calabrò<sup>60</sup>, L. Calacci<sup>66</sup>, Y. Camenen<sup>22</sup>, B. Cannas<sup>23</sup>, P. Cano Megías<sup>1</sup>, D. Carnevale<sup>66</sup>, F. Carpanese<sup>27</sup>, M. Carr<sup>7</sup>, D. Carralero<sup>9,59</sup>, L. Carraro<sup>16</sup>, A. Casolari<sup>36</sup>, A. Cathey<sup>9</sup>, F. Causa<sup>24</sup>, M. Cavedon<sup>9</sup>, M. Cecconello<sup>67</sup>, S. Ceccuzzi<sup>24</sup>, J. Cerovsky<sup>36</sup>, S. Chapman<sup>68</sup>, P. Chmielewski<sup>26</sup>, D. Choi<sup>27</sup>, C. Cianfarani<sup>24</sup>, G. Ciraolo<sup>18</sup>, S. Coda<sup>27</sup>, R. Coelho<sup>11</sup>, L. Colas<sup>18</sup>, D. Colette<sup>18</sup>, L. Cordaro<sup>16</sup>, F. Cordella<sup>24</sup>, S. Costea<sup>28</sup>, D. Coster<sup>9</sup>, D. J. Cruz Zabala<sup>1</sup>, G. Cseh<sup>69</sup>, A. Czarnecka<sup>26</sup>, I. Cziegler<sup>31</sup>, O. D'Arcangelo<sup>24</sup>, A. Dal Molin<sup>8</sup>, P. David<sup>9</sup>, G. De Carolis<sup>66</sup>, H. De Oliveira<sup>27</sup>, J. Decker<sup>27</sup>, R. Dejarnac<sup>36</sup>, R. Delogu<sup>16</sup>, N. den Harder<sup>37</sup>, M. Dimitrova<sup>36</sup>, F. Dolizy<sup>15</sup>, J. J. Domínguez-Palacios Durán<sup>1</sup>, D. Douai<sup>18</sup>, A. Drenik<sup>9</sup>, M. Dreval<sup>34</sup>, B. Dudson<sup>31</sup>, D. Dunai<sup>69</sup>, B. P. Duval<sup>27</sup>, R. Dux<sup>9</sup>, S. Elmore<sup>7</sup>, O. Embréus<sup>51</sup>, B. Erdős<sup>58</sup>, E. Fable<sup>9</sup>, M. Faitsch<sup>9</sup>, A. Fanni<sup>23</sup>, M. Farnik<sup>36</sup>, I. Faust<sup>9</sup>, J. Faustin<sup>37</sup>, N. Fedorczak<sup>18</sup>, F. Felici<sup>27</sup>, S. Feng<sup>8</sup>, X. Feng<sup>40</sup>, J. Ferreira<sup>11</sup>, G. Ferrò<sup>24</sup>, O. Février<sup>27</sup>, O. Ficker<sup>36</sup>, L. Figini<sup>8</sup>, A. Figueiredo<sup>11</sup>, A. Fil<sup>31</sup>, M. Fontana<sup>27</sup>, M. Francesco<sup>66</sup>, C. Fuchs<sup>9</sup>, S. Futatani<sup>2</sup>, L. Gabellieri<sup>24</sup>, D. Gadariya<sup>59</sup>, D. Gahle<sup>70</sup>, D. Galassi<sup>27</sup>, K. Galazka<sup>26</sup>, J. Galdon-Quiroga<sup>1</sup>, S. Galeani<sup>31</sup>, D. Gallart<sup>39</sup>, A. Gallo<sup>22</sup>, C. Galperti<sup>27</sup>, S. Garavaglia<sup>8</sup>, J. Garcia<sup>18</sup>, J. Garcia-Lopez<sup>1</sup>, M. Garcia-Munoz<sup>1</sup>, L. Garzotti<sup>7</sup>, J. Gath<sup>46</sup>, B. Geiger<sup>9</sup>, L. Giacomelli<sup>8</sup>, L. Giannone<sup>9</sup>, S. Gibson<sup>27</sup>, L. Gil<sup>11</sup>, E. Giovannozzi<sup>24</sup>, G. Giruzzi<sup>18</sup>, M. Gobbin<sup>16</sup>, J. Gonzalez-Martin<sup>1</sup>, T. P. Goodman<sup>27</sup>, G. Gorini<sup>25</sup>, M. Gospodarczyk<sup>66</sup>, G. Granucci<sup>8</sup>, D. Grekov<sup>33</sup>, G. Grenfell<sup>16</sup>, M. Griener<sup>9</sup>, M. Groth<sup>1</sup>, O. Grover<sup>36</sup>, M. Gruca<sup>26</sup>, A. Gude<sup>9</sup>, L. Guimaraes<sup>11</sup>, T. Gyergyek<sup>71</sup>, P. Hacek<sup>36</sup>, A. Hakola<sup>41</sup>, C. Ham<sup>7</sup>, T. Happel<sup>9</sup>, J. Harrison<sup>7</sup>, A. Havranek<sup>36</sup>, J. Hawke<sup>27</sup>, S. Henderson<sup>70</sup>, L. Hesslow<sup>51</sup>, F. Hitzler<sup>9</sup>, B. Hnat<sup>7,64</sup>, J. Hobirk<sup>9</sup>, M. Hoelzl<sup>9</sup>, D. Hogeweyj<sup>72</sup>, C. Hopf<sup>9</sup>, M. Hoppe<sup>51</sup>, J. Horacek<sup>36</sup>, M. Hron<sup>36</sup>, Z. Huang<sup>27,37</sup>, A. Iantchenko<sup>27</sup>, D. Iglesias<sup>7</sup>, V. Igochine<sup>9</sup>, P. Innocente<sup>16</sup>, C. Ionita-Schrittwieser<sup>28</sup>, H. Isliker<sup>73</sup>, I. Ivanova-Stanik<sup>26</sup>, A. Jacobsen<sup>7,9</sup>, M. Jakubowski<sup>37</sup>, F. Janky<sup>9</sup>, A. Jardin<sup>7,26</sup>, F. Jaulmes<sup>36</sup>, T. Jensen<sup>46</sup>, T. Jonsson<sup>38</sup>, A. Kallenbach<sup>9</sup>, A. Kappatou<sup>9</sup>, A. Karpushov<sup>27</sup>, S. Kasilov<sup>45</sup>, Y. Kazakov<sup>50</sup>, P. V. Kazantzidis<sup>74</sup>, D. Keeling<sup>7</sup>, M. Kelemen<sup>71</sup>, A. Kendl<sup>28</sup>, W. Kernbichler<sup>45</sup>, A. Kirk<sup>7</sup>, G. Kocsis<sup>69</sup>, M. Komm<sup>36</sup>, M. Kong<sup>27</sup>, V. Korovin<sup>34</sup>, M. Koubiti<sup>22</sup>, J. Kovacic<sup>71</sup>, N. Krawczyk<sup>26</sup>, K. Krieger<sup>9</sup>, L. Kripner<sup>36</sup>, A. Křivská<sup>50</sup>, O. Kudlacek<sup>9</sup>, Y. Kulyk<sup>34</sup>, T. Kurki-Suonio<sup>6</sup>, R. Kwiatkowski<sup>75</sup>, F. Laggner<sup>76</sup>, L. Laguardia<sup>8</sup>, A. Lahtinen<sup>77</sup>, P. Lang<sup>9</sup>, J. Likonen<sup>41</sup>, B. Lipschultz<sup>31</sup>, F. Liu<sup>78</sup>, R. Lombroini<sup>60</sup>, R. Lorenzini<sup>16</sup>, V. P. Loschiavo<sup>62</sup>, T. Lunt<sup>9</sup>, E. Macusova<sup>36</sup>, J. Madsen<sup>46</sup>, R. Maggiore<sup>79</sup>, B. Maljaars<sup>15</sup>, P. Manas<sup>9</sup>, P. Mantica<sup>8</sup>, M. J. Mantsinen<sup>39,80</sup>, P. Manz<sup>9</sup>, M. Maraschek<sup>9</sup>, V. Marchenko<sup>81</sup>, C. Marchetto<sup>8</sup>, A. Mariani<sup>8</sup>, C. Marini<sup>27</sup>, T. Markovic<sup>36</sup>, L. Marrelli<sup>16</sup>, P. Martin<sup>16</sup>, J. R. Martín Solís<sup>59</sup>, A. Martitsch<sup>45</sup>, S. Mastrostefano<sup>63,82</sup>, F. Matos<sup>37</sup>, G. Matthews<sup>7</sup>, M. -L. Mayoral<sup>65</sup>, D. Mazon<sup>18</sup>, C. Mazzotta<sup>24</sup>, P. Mc Carthy<sup>83</sup>, K. McClements<sup>7</sup>, R. McDermott<sup>9</sup>, B. Mcmillan<sup>68</sup>, C. Meineri<sup>16</sup>, V. Menkovski<sup>15</sup>, D. Meshcheriakov<sup>9</sup>, M. Messmer<sup>15</sup>, D. Micheletti<sup>8</sup>, D. Milanese<sup>79</sup>, F. Militello<sup>7</sup>, I. G. Miron<sup>84</sup>, J. Mlynar<sup>36</sup>, V. Moiseenko<sup>34</sup>, P. A. Molina Cabrera<sup>27</sup>, J. Morales<sup>18</sup>, J. -M. Moret<sup>27</sup>, A. Moro<sup>8</sup>, D. Moulton<sup>7</sup>, F. Nabais<sup>11</sup>,**

V. Naulin<sup>46</sup>, D. Naydenkova<sup>36</sup>, R. D. Nem<sup>46</sup>, F. Nespoli<sup>18,22</sup>, S. Newton<sup>7</sup>, A. H. Nielsen<sup>46</sup>, S. K. Nielsen<sup>46</sup>, V. Nikolaeva<sup>11</sup>, M. Nocente<sup>25</sup>, S. Nowak<sup>8</sup>, M. Oberkofler<sup>9</sup>, R. Ochoukov<sup>9</sup>, P. Ollus<sup>6</sup>, J. Olsen<sup>46</sup>, J. Omotani<sup>51</sup>, J. Ongena<sup>45</sup>, F. Orain<sup>9</sup>, F. P. Orsitto<sup>82</sup>, R. Paccagnella<sup>16</sup>, A. Palha<sup>15</sup>, L. Panaccione<sup>82</sup>, R. Panek<sup>36</sup>, M. Panjan<sup>71</sup>, G. Papp<sup>9</sup>, I. Paradela Perez<sup>6</sup>, F. Parra<sup>7,64</sup>, M. Passeri<sup>66</sup>, A. Pau<sup>6,27</sup>, G. Pautasso<sup>9</sup>, R. Pavlichenko<sup>34</sup>, A. Perek<sup>72</sup>, V. Pericoli Radolfini<sup>63</sup>, F. Pesamosca<sup>27</sup>, M. Peterka<sup>36</sup>, V. Petrzilka<sup>36</sup>, V. Piergotti<sup>82</sup>, L. Pigatto<sup>16</sup>, P. Piovesan<sup>16</sup>, C. Piron<sup>16</sup>, L. Piron<sup>7,16</sup>, V. Plyusnin<sup>11</sup>, G. Pokol<sup>58</sup>, E. Poli<sup>9</sup>, P. Pölöskei<sup>58</sup>, T. Popov<sup>85</sup>, Z. Popovic<sup>59</sup>, G. Pór<sup>58</sup>, L. Porte<sup>27</sup>, G. Pucella<sup>82</sup>, M. E. Puiatti<sup>16</sup>, T. Pütterich<sup>9</sup>, M. Rabinski<sup>75</sup>, J. Juul Rasmussen<sup>46</sup>, J. Rasmussen<sup>46</sup>, G. A. Rattá<sup>59</sup>, S. Ratynskaia<sup>38</sup>, T. Ravensbergen<sup>15</sup>, D. Réfy<sup>69</sup>, M. Reich<sup>9</sup>, H. Reimerdes<sup>27</sup>, F. Reimold<sup>19,37</sup>, D. Reiser<sup>19</sup>, C. Reux<sup>18</sup>, S. Reznik<sup>71</sup>, D. Ricci<sup>8</sup>, N. Rispoli<sup>8</sup>, J. F. Rivero-Rodriguez<sup>7</sup>, G. Rocchi<sup>82</sup>, M. Rodriguez-Ramos<sup>1</sup>, A. Romano<sup>82</sup>, J. Rosato<sup>44</sup>, G. Rubinacci<sup>82</sup>, G. Rubino<sup>16</sup>, D. A. Ryan<sup>7</sup>, M. Salewski<sup>46</sup>, A. Salmi<sup>41</sup>, D. Samaddar<sup>7</sup>, L. Sanchis-Sanchez<sup>1</sup>, J. Santos<sup>11</sup>, K. Särkimäki<sup>6</sup>, M. Sassano<sup>66</sup>, O. Sauter<sup>27</sup>, R. Scannell<sup>7</sup>, M. Scheffer<sup>15</sup>, B. S. Schneider<sup>28</sup>, P. Schneider<sup>9</sup>, R. Schrittwieser<sup>28</sup>, M. Schubert<sup>9</sup>, J. Seidl<sup>36</sup>, E. Seliunin<sup>11</sup>, S. Sharapov<sup>7</sup>, R. R. Sheeba<sup>22</sup>, G. Sias<sup>23</sup>, B. Sieglin<sup>9</sup>, C. Silva<sup>11</sup>, S. Sipilä<sup>6</sup>, S. Smith<sup>31</sup>, A. Snicker<sup>6</sup>, E. R. Solano<sup>59</sup>, S. K. Hansen<sup>46</sup>, C. Soria-Hoyo<sup>1</sup>, E. Sorokovoy<sup>34</sup>, C. Sozzi<sup>8</sup>, A. Sperduti<sup>67</sup>, G. Spizzo<sup>16</sup>, M. Spolaore<sup>16</sup>, M. Stejner<sup>46</sup>, L. Stipan<sup>27</sup>, J. Stober<sup>9</sup>, P. Strand<sup>51</sup>, H. Sun<sup>7,9</sup>, W. Suttrop<sup>9</sup>, D. Sytnykov<sup>34</sup>, T. Szepesi<sup>69</sup>, B. Tál<sup>69</sup>, T. Tala<sup>41</sup>, G. Tardini<sup>9</sup>, M. Tardocchi<sup>8</sup>, A. Teplukhina<sup>27</sup>, D. Terranova<sup>16</sup>, D. Testa<sup>27</sup>, C. Theiler<sup>27</sup>, E. Thorén<sup>38</sup>, A. Thornton<sup>7</sup>, B. Tilia<sup>24</sup>, P. Talias<sup>38</sup>, M. Tomes<sup>36</sup>, M. Toscano-Jimenez<sup>1</sup>, C. Tsironis<sup>74</sup>, C. Tsui<sup>27</sup>, O. Tudisco<sup>24</sup>, J. Urban<sup>36</sup>, M. Valisa<sup>16</sup>, M. Vallar<sup>16</sup>, P. Vallejos Olivares<sup>38</sup>, M. Valovic<sup>7</sup>, D. Van Vugt<sup>15</sup>, B. Vanovac<sup>72</sup>, J. Varje<sup>6</sup>, J. Varju<sup>36</sup>, S. Varoutis<sup>33</sup>, S. Vartanian<sup>18</sup>, O. Vasilovici<sup>28</sup>, J. Vega<sup>59</sup>, G. Verdoolaege<sup>51</sup>, K. Verhaegh<sup>27,31</sup>, L. Vermare<sup>44</sup>, N. Vianello<sup>16</sup>, J. Vicente<sup>11</sup>, E. Viezzer<sup>1</sup>, F. Villone<sup>82</sup>, I. Voitsekhovitch<sup>7</sup>, D. Voltolina<sup>16</sup>, P. Vondracek<sup>36</sup>, N. M. T. Vu<sup>27</sup>, N. Walkden<sup>7</sup>, T. Wauters<sup>50</sup>, M. Weiland<sup>9</sup>, V. Weinzettl<sup>36</sup>, M. Wensing<sup>27</sup>, S. Wiesen<sup>19</sup>, M. Wiesenberger<sup>28</sup>, G. Wilkie<sup>51</sup>, M. Willensdorfer<sup>9</sup>, M. Wischmeier<sup>9</sup>, K. Wu<sup>60</sup>, L. Xiang<sup>46</sup>, R. Zagorski<sup>26</sup>, D. Zaloga<sup>75</sup>, P. Zanca<sup>16</sup>, R. Zaplotnik<sup>11</sup>, J. Zebrowski<sup>75</sup>, W. Zhang<sup>9</sup>, A. Zisis<sup>74</sup>, S. Zoletnik<sup>69</sup> & M. Zuin<sup>16</sup>

<sup>62</sup>University of Napoli 'Federico II', Consorzio CREATE, Naples, Italy. <sup>63</sup>University of Napoli Parthenope, Consorzio CREATE, Naples, Italy. <sup>64</sup>Rudolf Peierls Centre for Theoretical Physics, University of Oxford, Oxford, UK. <sup>65</sup>EUROfusion PMU, Garching, Germany. <sup>66</sup>University of Rome Tor Vergata, Rome, Italy. <sup>67</sup>Department of Physics and Astronomy, Uppsala University, Uppsala, Sweden. <sup>68</sup>Department of Physics, Centre for Fusion, Space and Astrophysics, Warwick University, Coventry, UK. <sup>69</sup>Wigner Research Centre for Physics, Budapest, Hungary. <sup>70</sup>Department of Physics, University of Strathclyde, Glasgow, UK. <sup>71</sup>Jožef Stefan Institute, Ljubljana, Slovenia. <sup>72</sup>FOM Institute DIFFER, Eindhoven, the Netherlands. <sup>73</sup>Aristotle University of Thessaloniki, Thessaloniki, Greece. <sup>74</sup>National Technical University of Athens, Athens, Greece. <sup>75</sup>NCBJ National Centre for Nuclear Research, Otwock, Poland. <sup>76</sup>Institut für Angewandte Physik, Technische Universität Wien, Wien, Austria. <sup>77</sup>Department of Physics, University of Helsinki, Helsinki, Finland. <sup>78</sup>Université de Nice Sophia Antipolis, Nice, France. <sup>79</sup>Dipartimento di Elettronica e Telecomunicazioni, Politecnico di Torino, Turin, Italy. <sup>80</sup>ICREAP, Barcelona, Spain. <sup>81</sup>Fusion Theory Division, Institute for Nuclear Research of NAS, Kyiv, Ukraine. <sup>82</sup>ENEA/CREATE, DIEI, Università di Cassino, Cassino, Italy. <sup>83</sup>University College Cork, Cork, Ireland. <sup>84</sup>National Institute for Laser, Plasma and Radiation Physics, Bucharest, Romania. <sup>85</sup>Faculty of Physics, St. Kliment Ohridski University, Sofia, Bulgaria.

## Methods

### Nonlinear hybrid kinetic–MHD model MEGA and simulation setup

The hybrid kinetic–MHD simulations of ELMs presented in this manuscript have been performed with the code MEGA<sup>34</sup>. MEGA calculates the interaction between MHD instabilities and energetic particles self-consistently by adopting a drift-kinetic description<sup>51–53</sup> that couples the nonlinear MHD equations, which evaluate bulk plasma dynamics, with a  $\delta f$  method that describes the energetic particle population. In the hybrid simulations, finite Larmor radius effects of energetic particles are included by using the standard technique of four-point gyroaveraging around a particle's guiding centre<sup>54</sup>.

The equilibrium profiles that are used as initial conditions for the bulk plasma and geometry are taken from AUG shot #33616 at 7.2 s, just before the ELM crash (that is, pre-ELM)<sup>35</sup>. Extended Data Fig. 2 shows the profiles of the thermal electron density ( $n_e$ ), thermal electron temperature ( $T_e$ ) and the safety factor ( $q$ ) as a function of the radial coordinate  $\rho_{\text{pol}}$ . Here,  $\rho_{\text{pol}} = \sqrt{\psi_N}$  with  $\psi_N$  being the normalized poloidal flux with respect to the last closed magnetic flux surface. The pressure-constrained pre-ELM equilibrium has been reconstructed with the CLISTE code<sup>55</sup>. Extended Data Fig. 2a shows the experimental uncertainties of  $n_e$ ,  $T_e$  and  $q$ . The error bars of  $q$  at the core ( $\rho_{\text{pol}} < 0.3$ ) are not well defined because of the limitation of the available diagnostics. However, such error bars at the core do not affect the observations at the edge of the plasma reported in this paper. In the MEGA simulations presented here, the resistivity is given by  $\eta(T) = \eta_0(T/T_0)^{-3/2}$ , where  $T_0 = T_{e,0} + T_{i,0} = 6.6$  keV is the temperature and  $\eta_0 = 10^{-7} \Omega \text{m} \approx 20 \times \eta_{\text{Spitzer}}$  is the resistivity, both at the magnetic axis. The viscosity follows the same profile, leading to a constant magnetic Prandtl number,  $\text{Pr}_m = \frac{\nu}{\eta/\mu_0} = 10$ . The perpendicular thermal diffusivity is inferred from charge exchange measurements with  $\chi_{\perp,0} = 3.6 \text{ m}^2 \text{ s}^{-1}$  and a radial profile that mimics an edge transport barrier<sup>56,57</sup>. The parallel thermal diffusivity is given by the ratio  $\chi_{\parallel,0}/\chi_{\perp,0} = 10^5$  at the magnetic axis, as used in previous ELM simulations<sup>18</sup>, and with a radial dependency given by  $\chi_{\parallel} = \chi_{\parallel,0} \times (T/T_0)^{5/2}$  (ref. 58). Notice that both the MHD and hybrid kinetic–MHD simulations shown in this work consider the same resistivity, parallel and perpendicular thermal diffusivity profiles to highlight the impact of fast-ion kinetic effects on ELMs. Moreover, the impact of parallel gradients on the fast-ion kinetic effects on ELMs reported in this work is negligible because, in the MEGA code<sup>34</sup>, the effect of energetic particles on the thermal plasma is accounted for in the MHD momentum equation of the thermal plasma through the energetic particle force term,  $-\mathbf{j}_h \times \mathbf{B}$ , which acts in the direction perpendicular to the magnetic field. In addition, the fast-ion distribution considered in the simulations is toroidally axisymmetric.

The initial fast-ion distribution is modelled as an off-axis slowing-down NBI energetic ion distribution. The spatial dependence of the fast-ion distribution is given by the fast-ion pressure profile as

$$p_{\text{EP}} = \beta_{\text{EP}} \frac{B_0^2}{2\mu_0} \exp \left[ - \left( \frac{\psi_N - \psi_{N_0}}{\sigma_{\psi_N}} \right)^2 \right], \quad (3)$$

and the slowing-down NBI component is given by

$$I(v, \Lambda) = \frac{1}{v^3 + v_{\text{crit}}^3} \frac{1}{2} \text{erfc} \left( \frac{v - v_{\text{birth}}}{\Delta v} \right) \exp \left[ - \left( \frac{\Lambda - \Lambda_0}{\Delta \Lambda} \right)^2 \right]. \quad (4)$$

In equations (3) and (4),  $\beta_{\text{EP}} = 0.01$  is the ratio between fast-ion pressure peak and magnetic pressure,  $\mu_0 = 4\pi \times 10^{-7} \text{ H m}^{-1}$  is the vacuum magnetic permeability,  $B_0 = 2.5 \text{ T}$  is the magnetic field at the magnetic axis,  $\psi_N$  is the normalized poloidal flux,  $\psi_{N_0} = 0.55$  is the centre of the

off-axis,  $\sigma_{\psi_N} = 0.3$  is the spatial width,  $v_{\text{crit}}$  is the critical velocity for the collisional friction of fast ions with thermal electrons and ions being equal<sup>59</sup>,  $v_{\text{birth}}$  is the NBI injection velocity,  $\text{erfc}$  denotes the complementary error function,  $\Delta v = 0.05v_A$  is the distribution width in velocity space,  $v_A = 4.4 \times 10^6 \text{ ms}^{-1}$  is the Alfvén speed at the magnetic axis,  $\Lambda_0 = 0.5$  is the pitch angle for the distribution peak and  $\Delta \Lambda = 0.2$  is the distribution width. Extended Data Fig. 2a also shows the energetic particle pressure ( $p_{\text{EP}}$ ) profile. The initial fast-ion distribution in energy ( $E$ ) and normalized pitch-angle ( $\Lambda = \mu B_0/E$ ) space is shown in Extended Data Fig. 2b. A realistic fast-ion distribution in position and velocity space has been implemented using the analytical formula shown in this section. For the sake of clarity, to isolate the interaction between fast ions and ELMs, and to save computing resources in the simulations presented here, the fast-ion density in the plasma core has been artificially reduced and maximized at the edge. Single- $n$  hybrid simulations with a realistic fast-ion distribution in the region of interest ( $\rho_{\text{pol}} > 0.5$ ) as calculated with the TRANSP code<sup>60,61</sup> have been carried out to check that this simplified distribution does not affect the findings presented in this Article.

In MEGA, the time evolution is calculated using the fourth-order explicit Runge–Kutta method, and the spatial derivatives are evaluated using a fourth-order finite difference scheme. The boundary conditions are periodic in the toroidal direction. At the boundaries of the simulation domain, the perfect conducting no-slip wall boundary conditions are applied. In the simulations reported in this Article, the grid resolution is  $N_R \times N_\phi \times N_z = 512 \times 16 \times 512$  in the single- $n$  and  $N_R \times N_\phi \times N_z = 512 \times 160 \times 512$  in the multi- $n$  simulations, respectively. The time step is  $\Delta t = 4.2 \times 10^{-11} \text{ s}$ , and the number of computational particles for the kinetic module is  $N_{\text{CP}} = 1.8 \times 10^6$  in the single- $n$  simulations; in multi- $n$  simulations,  $N_{\text{CP}} = 1.8 \times 10^7$ . In the single- $n$  simulations, the toroidal angle ranges from 0 to  $2\pi/N$ , with  $N = 10$ . In the multi- $n$  simulations, the toroidal angle ranges from 0 to  $2\pi$ . Therefore, in the multi- $n$  simulations, the volume enclosed by the simulation domain is ten times larger than in the single- $n$  simulations. A Fourier filter is applied in the simulations and, therefore, only mode numbers  $n = 0$  and 10 are studied in the single- $n$  simulations, whereas all  $n = 0, \dots, 10$  modes are retained in the multi- $n$  simulations. The digital filter (smoother + compensator) described in page 438 of ref. 62 is applied in the simulations to reduce the numerical noise.

### FILD

The scintillator-based FILD acts as magnetic spectrogram and uses the magnetic field to scatter charged particles that then impact on different positions on a scintillator plate, depending on their energy and pitch angle<sup>29,63</sup>. The light emitted by the scintillator material is directed by means of an optical setup to the data acquisition systems. The light beam is divided with a beam splitter and guided to a photomultiplier array and to a charge-coupled device camera. The measurements from the photomultiplier array with a high temporal resolution (down to 1  $\mu\text{s}$ ) are used in this work to analyse the fast-ion losses during an ELM cycle. The FILD spectrogram shown in this Article has a temporal resolution of 512  $\mu\text{s}$  and a frequency resolution about 30 Hz. The spatial resolution of FILD is not defined because it is placed at a fixed location.

### Magnetic spectrograms

Magnetic pick-up coils are one of the basic diagnostics to track MHD instabilities by measuring magnetic field perturbations<sup>64,65</sup>. The measurement principle is based on Faraday's law; a voltage is induced in a wire loop when immersed into a temporally varying magnetic field. The Fourier transformation of the coil signals provides magnetic frequency spectrograms that allow to identify the frequency of the MHD instability. At AUG, several magnetic pick-up coil arrays are installed at the low field side and at the high field side of the tokamak and allow instabilities with frequencies up to 2 MHz to be detected. The magnetic spectrogram shown in this work has a temporal resolution of 256  $\mu\text{s}$ ,

and its frequency resolution is about 30 Hz. The spatial resolution of this diagnostic is not defined because it is placed at a fixed location.

### ELM synchronization method

The measured data from magnetic pick-up coils and FILD measurements are synchronized with respect to the ELM onset times. To this end, the divertor shunt current measurements are first used to identify the onset times of individual ELM crashes within a given time window of a discharge. From these measurements, the ELM crashes become apparent as spikes in the signal because heat and particles flushed out by the ELMs increase the currents flowing onto the divertor. The start times of the ELM crashes are then determined by the onset of the rise of the shunt current signal. Once the ELM start times are identified, a correlation analysis of the shunt current rise profiles is performed. This is done to select only those ELMs with similar characteristics for synchronization. Here, only ELMs with a correlation factor above 0.7 with respect to the initial ELM crash in the time window are selected. In this way, small ELMs and other small plasma bursts are ignored. Once a set of the most similar ELMs has been identified, a new time base for the ELM-synchronized signal is created. This is done by subtracting the selected ELM onset times from the original time base of the corresponding signal and rearranging the data chronologically. In this way, timepoint 0 in the synchronized time base corresponds to the ELM onset time, with negative and positive timepoints corresponding to the times before and after the ELM onset, respectively.

### Data availability

The experimental data that support the findings of this study belong to AUG (shot #33616) and EUROfusion MST1 (AUG shot #37700) teams. They are available from the corresponding authors upon reasonable request. The simulation data that support the outcome of this work are available from the corresponding authors upon reasonable request.

### Code availability

The hybrid code MEGA can be made available upon reasonable request to the corresponding authors and with permission of the original author of the code, Y.T., at National Institute for Fusion Science (tohdo.yasushi@nifs.ac.jp).

### References

- Parker, S. E. et al. A fully nonlinear characteristic method for gyrokinetic simulation. *Phys. Fluids B* **5**, 77–86 (1993).
- Dimits, A. M. et al. Partially linearized algorithms in gyrokinetic particle simulation. *J. Comput. Phys.* **107**, 309–323 (1993).
- Aydemir, A. Y. A unified Monte Carlo interpretation of particle simulations and applications to non-neutral plasmas. *Phys. Plasmas* **1**, 822–831 (1994).
- Lee, W. W. Gyrokinetic particle simulation model. *J. Comput. Phys.* **72**, 243–269 (1987).
- McCarthy, P. J. Analytical solutions to the Grad–Shafranov equation for tokamak equilibrium with dissimilar source functions. *Phys. Plasmas* **6**, 3554–3560 (1999).
- Viezza, E. et al. Ion heat transport dynamics during edge localized mode cycles at ASDEX Upgrade. *Nucl. Fusion* **58**, 026031 (2018).
- Viezza, E. et al. Dynamics of the pedestal transport during edge localized mode cycles at ASDEX Upgrade. *Plasma Phys. Control. Fusion* **62**, 024009 (2020).
- Braginskii, S. I. Transport processes in plasma. *Rev. Plasma Phys.* **1**, 205–311 (1965).
- ITER Physics Expert Group on Energetic Particles, Heating and Current Drive & ITER Physics Basis Editors. ITER Physics Basis Chapter 5: Physics of energetic ions. *Nucl. Fusion* **39**, 2471–2495 (1999).

- Hawryluk, R. J. An empirical approach to tokamak transport. In *Physics of Plasmas Close to Thermonuclear Conditions* (eds Coppi, B. et al.) 19–46 (Pergamon, 1981).
- Pankin, A. et al. The tokamak Monte Carlo fast ion module NUBEAM in the National Transport Code Collaboration library. *Comput. Phys. Commun.* **159**, 157–184 (2004).
- Birdsall, C. K. & Langdon, A. B. *Plasma Physics Via Computer Simulation* (Taylor & Francis, 2005).
- Zweben, S. J. et al. Pitch angle resolved measurements of escaping charged fusion products in TFTR. *Nucl. Fusion* **29**, 825–833 (1989).
- Strait, E. J. et al. Chapter 2: magnetic diagnostics. *Fusion Sci. Technol.* **53**, 304–334 (2008).
- Brusati, M. et al. Analysis of magnetic measurements in tokamaks. *Comput. Phys. Rep.* **1**, 345–372 (1984).
- Fischer, R. et al. Estimation and uncertainties of profiles and equilibria for fusion modeling codes. *Fusion Sci. Technol.* **76**, 879–893 (2020).

### Acknowledgements

We thank A. Kallenbach, H. Zohm, K. Ichiguchi, A. Loarte, M. Hoelzl and M. Dunne for fruitful discussions and for their valuable input. This work received funding from the Spanish Ministry of Science (grant nos. FPU17/05703 and PID2020-116822RB-I00). This work received funding from the European Research Council (ERC) under the European Union's Horizon 2020 research and innovation programme (grant agreement no. 805162). This work was supported by the NINS programme of Promoting Research by Networking among Institutions. This work has been carried out within the framework of the EUROfusion Consortium, funded by the European Union via the Euratom Research and Training Programme (grant agreement no. 101052200 – EUROfusion). Views and opinions expressed are, however, those of the author(s) only and do not necessarily reflect those of the European Union or the European Commission. Neither the European Union nor the European Commission can be held responsible for them. This work was co-funded by the European Regional Development Fund (Andalusian Operational Programme 2014–2020) and by the Ministry of Economic Transformation, Industry, Knowledge and Universities of the Junta de Andalucía within the framework of the PAIDI project with reference P18-FR-3812. We acknowledge the computer resources of RES (Spanish Supercomputing Network) at MareNostrum and the technical support provided by Barcelona Supercomputing Center (BSC) and the support from Marconi-Fusion, the High Performance Computer at the CINECA headquarters in Bologna (Italy) for its provision of supercomputer resources. We acknowledge PRACE for awarding us access to ARCHER2-HPC hosted by EPCC, UK. This work was carried out (partially) using JFRS-1 supercomputer resources at the Computational Simulation Centre of International Fusion Energy Research Centre (IFERC-CSC) in Rokkasho Fusion Institute of QST, provided under the EU-JA Broader Approach collaboration.

### Author contributions

J.D.-P.: methodology, software, validation, formal analysis, investigation, data curation, writing (original draft, editing and reviewing) and visualization. S.F.: methodology, software, resources, writing (original draft, editing and reviewing) and supervision. M.G.-M.: conceptualization, resources, writing (original draft, editing and reviewing), supervision, project administration and funding acquisition. A.J.v.V.: software, formal analysis, resources, writing (original draft), investigation and visualization. E.V.: conceptualization, resources, writing (original draft, editing and reviewing), supervision and funding acquisition. J.G.-M.: software, resources and writing (original draft). M.T.-J.: methodology, writing (original draft, editing

and reviewing), supervision and project administration. P.O.: software, resources and writing (original draft). Y.T.: methodology, resources and writing (original draft). Y.S.: methodology, resources and writing (original draft). L.S.: investigation, resources and writing (original draft). J.R.-R.: software, investigation, formal analysis, visualization and writing (original draft). J.G.-Q.: investigation, formal analysis and writing (original draft). J.H.-S.: formal analysis, visualization and writing (original draft). H.C.: formal analysis and writing (original draft). J.F.R.-R.: formal analysis, investigation and writing (original draft). L.V.: formal analysis and investigation. AUG Team: writing (original draft) and resources. EUROfusion MST1 Team: writing (original draft) and resources.

### Competing interests

The authors declare no competing interests.

### Additional information

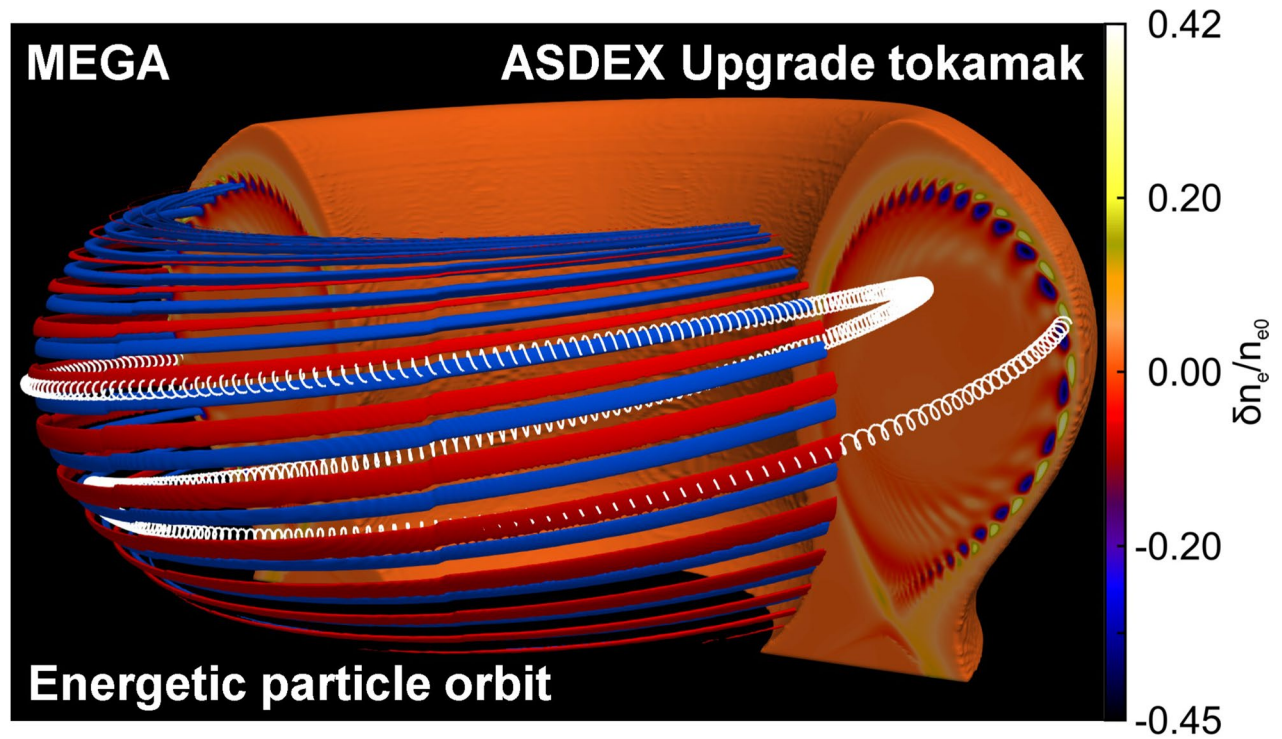
**Extended data** is available for this paper at <https://doi.org/10.1038/s41567-024-02715-6>.

**Supplementary information** The online version contains supplementary material available at <https://doi.org/10.1038/s41567-024-02715-6>.

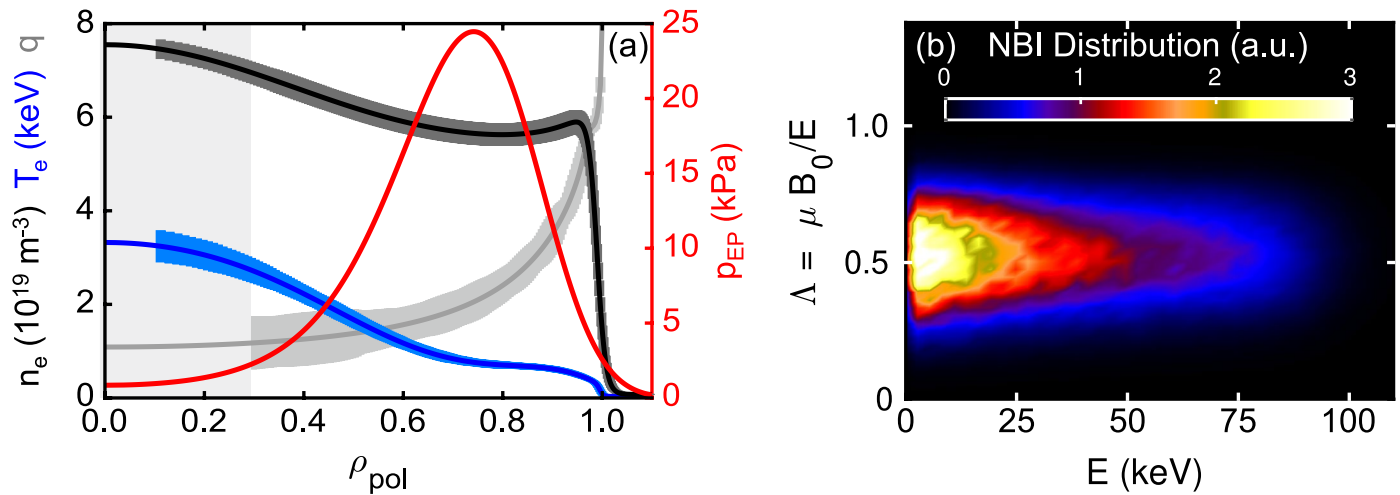
**Correspondence and requests for materials** should be addressed to J. Dominguez-Palacios or M. Garcia-Munoz.

**Peer review information** *Nature Physics* thanks Wei Chen, Chang Liu and X. Q. Xu for their contribution to the peer review of this work.

**Reprints and permissions information** is available at [www.nature.com/reprints](http://www.nature.com/reprints).



**Extended Data Fig. 1 | Energetic particle orbit in an ELM.** Schematic view of 3D illustration of an  $n = 10$  density perturbation (here,  $\delta n_e / \delta n_{e0}$ ), with  $\delta n_{e0}$  the equilibrium density profile) of an ELM in the ASDEX Upgrade (AUG) tokamak interacting with a mirror-trapped energetic particle (white solid curve) with energy  $E = 93$  keV.



**Extended Data Fig. 2 | Initial bulk plasma and energetic particle profiles.**

(a) Electron density (black), electron temperature (blue) and safety factor (grey) profiles for AUG shot #33616 at  $t = 7.2$  ms (left axis), including their error bars (blue, black and light and dark grey shaded areas, respectively), and initial fast-ion pressure profile (red, right axis). The x-axis represents the radial coordinate  $\rho_{\text{pol}} = \sqrt{\Psi_{\text{N}}}$ , where  $\Psi_{\text{N}}$  is the normalized poloidal flux. The error bars in the  $n_e$  and  $T_e$  profile reflect the standard deviation in the fitting of the experimental data,

whereas the error bars of the  $q$  profile are obtained using a bayesian approach as described in ref. 66. The error bars of the safety factor profile at the plasma core ( $\rho_{\text{pol}} < 0.3$ , light grey shaded area) are not well defined because of the limitation of the available diagnostics, contrary to the region  $\rho_{\text{pol}} > 0.3$  (dark grey shaded area). (b) Neutral Beam Injection (NBI) slowing down distribution in  $(E, \Lambda)$  space, where  $E$  is the energy and  $\Lambda = \mu B_0/E$  is the normalized pitch angle. Here,  $\mu$  is the magnetic moment and  $B_0$  the magnetic field at the magnetic axis.